



Synthesis and characterisation of nano-hybrid complexes for electrocatalysis

By

Sherilee Pillay

Submitted in fulfilment of the requirement for the degree of

Master of Science

In the Faculty of Natural and Agricultural Science,
University of Pretoria

June 2015

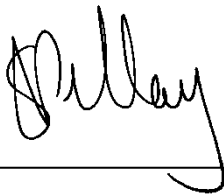
Supervisor Dr. J. Pillay

Co-Supervisor Prof. K. I. Ozoemena



DECLARATION

I, Sherilee Pillay, declare that the dissertation, which I hereby submit for the degree Magister Scientiae in the Faculty of Natural and Agricultural Sciences at the University of Pretoria, is my own work and has not previously been submitted by me for a degree at this or any other tertiary institution.



Sherilee Pillay

June 2015



DEDICATION

*To my family, thank you for the love and support you gave to me.
Thank you for never losing faith in me.*



ACKNOWLEDGEMENTS

I would like to acknowledge my supervisors Prof. K. Ozoemena and Dr. J. Pillay.

Prof. K. Ozoemena, I would like to express my sincere appreciation for your support and guidance. Your encouragement gave me the confidence and diligence to complete this work.

Dr. J. Pillay, I am grateful for your supervision and guidance. Thank you for the support. Your dedication, motivation and faith were the driving forces of this dissertation.

I wish to extend my appreciation to the management and scientists at MinteK (AuTEK Nanotechnology Laboratory) for allowing me to carry out my experiments in their lab and for all the support and teachings throughout my stay. Katlego Makgopa and Paul Ejikeme, thank you for the help during my research undertaken at The University of Pretoria, your teachings and guidance are greatly appreciated. To the National Research Foundation (NRF), thank you for the financial assistance. And a final thank you to the head of the chemistry department at the University of Pretoria, Prof Rowher for accepting my application for MSc.



ABSTRACT

Synthesis and characterisation of nano-hybrid complexes for electrocatalysis

By

Sherilee Pillay

Supervisor: Prof. K. Ozoemena

Co-Supervisor: Dr. J. Pillay

Submitted in the fulfilment of the requirements for the degree of Masters of Science, Department of Chemistry, University of Pretoria, Pretoria

Electrocatalysis is an influential field in electrochemistry that has seen significant growth due to the application and ever-emerging synthetic techniques. The electrocatalytic ability of multi-walled carbon nanotubes (MWCNT) integrated with nanostructured materials has been a key area of research. These integrated nanohybrids are carefully architected to produce complexes with new characteristics and properties that differ from their individual bulk components. These nanohybrids hold significance importance as they are used in various real world applications such as electrochemical reactions, organic electrosynthesis, fuel cells and battery preparation.



This thesis aimed to investigate the characteristics and electrocatalytic parameters of 3 synthesised nanohybrids. The structures of the hybrids were revealed using microscopic techniques (performed by TEM, UV, Zeta potential and AFM). Electrochemical studies were performed by voltammetric and electrochemical techniques. The initial hybrid formed was AuNP on MWCNT (AuNP/MWCNT hybrid), however during the electrocatalytic analysis, the hybrid showed inconsistent results therefore no further investigations were performed.

The second hybrid consisted of the integration of AuNR and MWCNT (AuNR/MWCNT hybrid), this hybrid showed a good current response compared to the bulk. Chronoamperometric experiments showed the k and D value were $6.71 \times 10^6 \text{ cm}^3 \text{ mol}^{-1} \text{ s}^{-1}$ and $1.69 \times 10^{-6} \text{ cm}^2 \text{ s}^{-1}$ respectively. The limit of detection (LoD) was calculated to be 0.5 s/m. No capacitive properties were investigated for this hybrid. A novel hybrid was also designed and synthesised using MWCNT and nCoTCPc (nCoTCPc/MWCNT). Chronoamperometric experiments showed that the k and D value were $17.88 \times 10^6 \text{ cm}^3 \text{ mol}^{-1} \text{ s}^{-1}$ and $2.51 \times 10^{-6} \text{ cm}^2 \text{ s}^{-1}$ respectively and the LoD as 3.3 s/m. The electron transfer rate constant was calculated $k_{\text{app}} = 19.73 \times 10^{-3} \text{ cm} \cdot \text{s}^{-1}$.

The nCoTCPc/MWCNT nanohybrid material exhibited an extra-ordinarily high conductivity ($15 \text{ mS} \cdot \text{cm}^{-1}$), which is more than an order of magnitude greater than that of the MWCNT ($527 \text{ } \mu\text{S} \cdot \text{cm}^{-1}$) and three orders of a magnitude greater than the nCoTCPc ($4.33 \text{ } \mu\text{S} \cdot \text{cm}^{-1}$). The heterogeneous electron transfer rate constant decreases as follows: nCoTCPc/MWCNT ($k_{\text{app}} \approx 19.73 \times 10^{-3} \text{ cm s}^{-1}$) > MWCNT (k_{app}



$\approx 11.63 \times 10^{-3} \text{ cm s}^{-1}$) > nCoTCPc ($k_{\text{app}} \approx 1.09 \times 10^{-3} \text{ cm.s}^{-1}$). The energy-storage capability was typical of pseudocapacitive behaviour; at a current density of $10 \mu\text{A.cm}^{-2}$, the pseudocapacitance decreases as nCoTCPc/MWCNT ($3.71 \times 10^{-4} \text{ F.cm}^{-2}$) > nCoTCPc ($2.57 \times 10^{-4} \text{ F.cm}^{-2}$) > MWCNT ($2.28 \times 10^{-4} \text{ F.cm}^{-2}$). The new nCoTCPc/MWCNT nanohybrid material promises to serve as a potential material for the fabrication of thin film electrocatalysts or energy-storage devices.



TABLE OF CONTENTS	PAGE
--------------------------	-------------

CHAPTER 1: INTRODUCTION

1.1 GENERAL OVERVIEW	2
1.2 ELECTROCHEMISTRY: AN OVERVIEW	4
1.2.1 BASIC CONCEPTS.....	6
1.2.1.1 THE ELECTROCHEMICAL CELL	6
1.2.1.2 MASS TRANSPORT	7
1.2.1.3 ELECTROCHEMICAL EQUILIBRIUM: INTRODUCTION.....	7
1.2.1.4 ELECTROCHEMICAL EQUILIBRIUM: ELECTRON TRANSFER AT THE ELECTRODE-SOLUTION INTERFACE	8
1.2.1.5 FARADAIC AND NON-FARADAIC PROCESSES	11
1.2.1.6 CLASSIFICATION OF ELECTROCHEMICAL TECHNIQUES.....	12
1.2.2 VOLTAMMETRY.....	12
1.2.2.1 CYCLIC VOLTAMMETRY.....	12
1.2.2.2 CHRONOAMPEROMETRY	17
1.2.2.3 GALVANOSTATIC MEASUREMENTS.....	18
1.2.2.4 ELECTROCATALYSIS	19
1.2.2.5 ELECTROCHEMICAL IMPEDANCE SPECTROSCOPY	20
1.3 MODIFIED ELECTRODES	24
1.3.1 METHODS OF MODIFYING ELECTRODE SURFACES.....	24
1.3.2 SELF-ASSEMBLED MONOLAYERS	25
1.3.3 LAYER BY LAYER SELF-ASSEMBLED MONOLAYERS	26



1.4 NANOPARTICLES.....	27
1.4.1 GOLD NANOPARTICLES	27
1.4.3 PHTHALOCYANINE.....	36
1.5 MICROSCOPIC TECHNIQUES	41
1.5.1 ELECTRON MICROSCOPY.....	41
1.5.2 ATOMIC FORCE MICROSCOPY	42
1.5.3 ULTRAVIOLET SPECTROSCOPY.....	42
CHAPTER 2: EXPERIMENTAL	
2.1 MATERIALS AND REAGENTS.....	44
2.2 ELECTRODE MODIFICATION AND PRE-TREATMENT.....	48
2.3 EXPERIMENTAL EQUIPMENT	49
CHAPTER 3: RESULTS AND DISCUSSION	
3.1 PRE-TREATMENT OF GOLD ELECTRODES	52
3.2 ANALYSIS OF HYBRIDS.....	53
3.2.1 AuNP/MWCNT HYBRID	53
3.2.2 AuNR/MWCNT HYBRID	55
3.2.3 nCoTCpC/MWCNT HYBRID	65
CONCLUSION	92
RECOMMENDATIONS.....	94



LIST OF ABBREVIATIONS

AFM	=	Atomic Force Microscopy
Ag AgCl	=	Silver silver Chloride Reference Electrode
CA	=	Chronoamperometry
CE	=	Counter Electrode
CME	=	Chemically Modified Electrode
CNT	=	Carbon Nanotubes
CoTCPC	=	Cobalt (II) Tetracarboxy-Phthalocyanine
CV	=	Cyclic Voltammetry
DMAET	=	Dimethylaminoethanethiol
EIS	=	Electrochemical Impedance Spectroscopy
KCL	=	Potassium Chloride
LoD	=	Limit of Detection
MPc	=	Metallophthalocyanine
MWCNT	=	Multiwalled Carbon Nanotube
PBS	=	Phosphate Buffer Solution
Pc	=	Phthalocyanine
R_{ct}	=	Charge Transfer Resistance
RE	=	Reference Electrode
R_s	=	Solution Resistance



SEM	=	Scanning Electron Microscopy
SWCNT	=	Single Walled Carbon Nanotubes
TEM	=	Transmission Electron Microscopy
UV-Vis	=	Ultraviolet-Visible
WE	=	Working Electrode
Z_w	=	Warburg Impedance



LIST OF FIGURES

Figure 1. 1	The integrated Gouy-Chapman-Stern model illustrating the three imaginary planes that are present in an electrical double layer ...	10
Figure 1. 2	Typical Cyclic Voltammogram for a reversible process	13
Figure 1. 3	Schematic diagram of the process of electrocatalysis	19
Figure 1. 4	The Randles equivalent circuit	22
Figure 1. 5	Typical EIS Nquist plot	23
Figure 1. 6	Illustration of (a) Single-walled carbon nanotubes (b) double-walled carbon nanotubes and (c) Multi-walled carbon nanotubes	32
Figure 1. 7	Illustrating the various CNT structures	33
Figure 1. 8	Illustration of a) the phthalocyanine complex (M= transition metals such as Cu, Co Ni etc.) and b) the phthalocyanine complex with R-Group substituent's.....	39
Figure 3. 1	Cyclic voltammogram in 0.5 M KOH illustrating the desorption profile of impurities off the gold electrode surface at 25 mV.s ⁻¹	52
Figure 3. 2	A typical Cyclic voltammogram of a freshly cleaned gold electrode surface at 25 mV.s ⁻¹ in 0.5 M H ₂ SO ₄	53
Figure 3. 3	TEM illustrations of (a) the AuNP/MWCNT hybrid (~x50k mag.)..	54
Figure 3. 4	UV Visible spectrum for (i) MWCNT, (ii) AuNP and (iii) AuNP/MWCNT hybrid in pH 7.4 PBS solution	54
Figure 3. 5	TEM image of AuNR assembled on MWCNT (~x50k mag.).....	56
Figure 3. 6	Comparative EIS parameter data obtained for Bare-Au, Au-MPA, Au-MPA-AuNR, Au-MPA-MWCNT and Au-MPA-AuNR/MWCNT in a (a) Cyclic voltammogram and (b) Nyquist plots in 0.1 KCl containing equimolar mixture of K ₄ Fe(CN) ₆ and K ₃ Fe(CN) ₆	59
Figure 3. 7	Cyclic voltammetric profiles of the different electrodes in the (a) absence and (b) presence of 50 μM EP in PBS pH 7.4 as a scan rate of 25 mVs ⁻¹	61
Figure 3. 8	(a) Cyclic voltammograms of increasing scan rates (5 – 300 mV.s ⁻¹) for 10 mM EP in PBS pH 7.4 for Au-MPA-AuNR/MWCNT (b) Plot of	



	peak current (I_p) vs. square root of scan rate ($v^{1/2}$) and (c) plot of peak potential (E_p) vs. log of scan rate (v) from scan rate data.. 62
Figure 3. 9	Typical double potential step chronoamperometric transients at Au-MPA-AuNR/MWCNT in pH 7.4 PBS solution following addition of epinephrine. Concentration range (0.47–4.12 μM). Inset shows the plot of chronoamperometric current at $t = 1.2 \text{ s}$ vs. $[\text{EP}]$ at a scan rate of $25 \text{ mV}\cdot\text{s}^{-1}$ 65
Figure 3. 10	TEM image of (a) CoTCPc (x6k mag.), (b) nCoTCPc (x50k mag.), (c)/(d) MWCNT (x10k mag.) and (e)/(f) nCoTCPc/MWCNT (x10k mag.) 66
Figure 3.11	UV-visible spectra of (i) nCoTCPc, (ii) MWCNT and (iii) nCoTCPc/MWCNT..... 67
Figure 3. 12	AFM images of (a)/(b) Bare gold electrode, and gold-modified with (c)/(d) MWCNT, (e)/(f) nCoTCPc, and (g)/(h) nCoTCPc/MWCNT at room temperature 69
Figure 3. 13	Comparative EIS parameter data obtained for Bare gold, and gold-modified with MPA, MWCNT, nCoTCPc and nCoTCPc/MWCNT in a (a) Cyclic voltammogram, (b) Nyquist plots and (c) Bode plots in 0.1 KCl containing equimolar mixture of $\text{K}_4\text{Fe}(\text{CN})_6$ and $\text{K}_3\text{Fe}(\text{CN})_6$... 72
Figure 3. 14	Comparative cyclic voltammograms of the Bare Au electrode, nCoTCPc and nCoTCPc/MWCNT modified electrodes in (a) acidic solution (1M H_2SO_4). Figure (b) depicts the scan rate studies in acidic solution 76
Figure 3. 15	(a) Galvanostatic charge/discharge curves obtained for (i) nCoTCPc, (ii) MWCNT, and (iii) nCoTCPc/MWCNT. Figure 3.15 (b) illustrates the SC of nCoTCPc/MWCNT at current densities of 10, 5 and $3 \mu\text{A}\cdot\text{cm}^{-2}$ 77
Figure 3. 16	Typical (a) Nquist plot and (b) Bode plots for MWCNT, nCoTCPc and nCoTCPc/MWCNT..... 80
Figure 3. 17	Stability and efficiency plots of the gold electrode modified with nCoTCPc/MWCNT obtained at $10\mu\text{A}\cdot\text{cm}^{-2}$ in 1.0 M H_2SO_4 81



Figure 3. 18	Cyclic voltammetric profiles of the different electrodes in (a) presence and (b) absence of 50 μM EP in pH 7.4 PBS at a scan rate of 25 $\text{mV}\cdot\text{s}^{-1}$ 82
Figure 3. 19	(a) Cyclic voltammograms of increasing scan rates (5 – 300 $\text{mV}\cdot\text{s}^{-1}$) for 10 mM EP in PBS pH 7.4 for Au-MPA-nCoTCPc/MWCNT (b) Plot of peak current (I_p) vs. square root of scan rate ($v^{1/2}$) and (c) plot of peak potential (E_p) vs. log of scan rate (v) from scan rate data.. 86
Figure 3. 20	Typical double potential step chronoamperometric at Au-MPA-nCoTCPc/MWCNT in pH 7.4 PBS solution following addition of epinephrine. Concentration range (0.47–4.12 μM). Insert shows the plot of chronoamperometric current at $t = 1.2$ s vs. [EP] at scan rate 25 $\text{mV}\cdot\text{s}^{-1}$ 90



LIST OF SCHEMES

Scheme 1. 1	A Schematic illustration of the preparation and modification of the nCoTCPc/MWCNT electrode. (1) Synthesis of nCoTCPc, (2) Synthesis of the functionalised MWCNT and (3) hybrid synthesis and electrode modification	47
-------------	--	----

LIST OF TABLES

Table 1. 1	Classification criteria for reversible, irreversible and quasi- reversible cyclic voltammetric processes	17
Table 3. 1	The zeta potential and conductivity values obtained for (a) MWCNT, (b) AuNR and (c) AuNR/MWCNT	57
Table 3. 2	The zeta potential and conductivity values obtained for (a) MWCNT, (b) AuNR and (c) AuNR/MWCNT	70
Table 3. 3	Summary of the electrochemical impedance spectroscopic evolutions for the electrodes in $[\text{Fe}(\text{CN})_6]^{3-}/[\text{Fe}(\text{CN})_6]^{4-}$ redox systems in 0.1 M KCl solution	74
Table 3. 4	Comparative data showing the specific capacitance, specific energy density and specific power density for the electrodes	79
Table 3. 5	Comparative analytical data for the detection of epinephrine using electrochemical techniques	89



CHAPTER ONE

INTRODUCTION



1.1 GENERAL OVERVIEW

Electrochemical sensors are very promising analytical tools because of their sensitivity, selectivity and stability. They are frequently used in biological analysis, medical engineering, process engineering and environmental analysis as they provide a useful and easy method in determination of concentrations and properties of various analytes. The technique has become a valued diagnostic tool for biological detection and measurement as it is simple, low-cost and can be designed and fabricated according to specific analytes. The success of these intricately architected devices depends on the electrode, the electrocatalyst and the application technique. Significant focus has been on developing complementary nanomaterials for these electrochemical devices to catalyse and amplify the signal.

This thesis describes the characteristics and electrocatalytic behaviour of multiwalled carbon nanotubes (MWCNT) modified with nanoparticles on bulk gold electrodes. The nanoparticles used were colloidal gold nanoparticles (AuNP), gold nanorods (AuNR) and nano-cobalt tetracarboxy phthalocyanine (nCoTCPC).



Aim of Thesis:

1. The synthesis and characterisation of nanohybrids composed of MWCNT and redox-active nanoparticles (AuNP, AuNR and nCoTCPc).
2. The modification of gold electrodes with (i) AuNP/MWCNT, (ii) AuNR/MWCNT and (iii) nCoTCPc/MWCNT
3. The investigation of the electrocatalytic ability of modified electrodes towards the detection of Epinephrine at a biological pH 7.
4. The investigation of the charge storage properties of the novel nCoTCPc/MWCNT hybrid.

In this introductory section, a general overview of the electrochemical techniques, carbon nanotubes (CNT), nanoparticles (NP) and metallophthalocyanine (MPc) will be discussed. Chapter 2 provides the details on the experimental work and is thereafter discussed in chapter 3.



1.2 ELECTROCHEMISTRY: AN OVERVIEW

Electrochemistry has been described as the fundamental study of the interplay of electricity and chemical reactions; it involves the measurement of electric quantities such as current, potential, and charge present during a chemical reaction. The transfer of electrons between different chemical species cause reactions that are specifically termed redox reactions and can be described by separating the reaction into two half reactions- the reduction and oxidation half reaction. The reduction half reaction is performed by the oxidizing agent; it gains electrons at the cathode and is reduced but promotes the proceeding oxidation process. The oxidation half reaction is performed by the reducing agent, it loses electrons at the anode and is oxidized but promotes reduction ^[1].

Fundamental electrochemical reactions are heterogeneous in nature as they take place at the electrode solution interface, this creates a phase boundary between the solute far from the electrode and those close enough to the surface of the electrode to participate in the electron transfer process ^[2-3]. The use of electrochemistry for analytical applications has a wide range of applications such as industrial quality control, biomedical analysis and environmental monitoring ^[4].

The work described in this thesis applies the electroanalytical techniques; cyclic voltammetry (CV), Chronoamperometry (CA) and Galvanostatic charge/discharge.



HISTORY

During the 16th century, magnetism was seen as the most important and investigated concept however it was during this time that electricity began to emerge as a significant concept. French chemist Charles Francois de Cisternay du Fay had discovered two types of static electricity during the 1700's, according to his investigations like charges repel each other while unlike charges attract ^[5-6]. In later years Charles-Augustin de Coulomb proposed his law of electrostatic attraction and was honoured for his contribution with the naming of one unit of charge a coulomb. It was at this time when insight into the new phenomenon of electricity was growing, that the integration of chemistry with electricity began developing. In the 1800s, London surgeon Anthony Carlisle and chemical engineer William Nicholson showed that an electrical circuit could decompose water into oxygen and hydrogen.

This was a significant discovery as it showed that a chemical reaction can be driven by an electrical current, a concept we refer to as electrolysis. Supporting work for this discovery was performed by Sir Humphry Davy's and it was concluded that the production of electricity in electrolytic cells results from chemical reactions and that chemical interactions occurred between substances of opposite charges. In later years, Micheal Faraday's work merged the understanding and knowledge of electricity, chemistry and day-to-day technology ^[7].

Faraday's concept of lines of flux coming from charged bodies and magnets provided a way to visualise electric and magnetic fields and was crucial to the successful development of electromechanical devices. His work with chemistry



involved the discovery of the laws of electrolysis, by which he quantified electrochemistry. In subsequent years, many scientists enhanced the understanding and optimization of the integration of chemistry and electricity [8].

1.2.1 BASIC CONCEPTS

1.2.1.1 THE ELECTROCHEMICAL CELL

Electrolytic cells consist of 3 electrodes: the working, auxiliary (or counter) and reference electrode. These electrodes are made from sufficiently conductive material such as; metals, semi-conductors, graphite or even conductive polymers. The three electrode system is used to study the behaviour of the analyte at the electrode-solution interface, at which both the potential and current is monitored. Initially the system must be taken away from the electrochemical equilibrium by applying a potential to the system which polarizes the working electrode. The potential range involved in the redox reaction and the kinetics of the electron transfers are factors to consider in the usage of working electrodes. The most commonly used working electrodes are carbon, gold and platinum electrodes [9-11].

The reference electrode acts as a reference point for the redox couple and is commonly made of metals such as platinum, gold, nickel, mercury, gold-amalgam or a variety of alloys [9]. These materials have excellent comparative standards as they carry no current and therefore won't alter the potential. When a fixed potential difference is applied between the working electrode and the reference electrode, electrochemical redox reactions will occur at the working electrode surface. The deviation from the equilibrium is then measured by recording the current that developed across the working and reference electrode.



The auxiliary electrode is required to complete the circuit as it carries current and acts as a source or sink of electrons in the circuit formed with the working electrode. By the addition of this third electrode, the potentiostat is able to pass current through the analyte solution without passing current into or out of the reference electrode thus the reference electrodes voltage variations due to electrode polarization or IR drops are eliminated. The counter electrode should be made of an electrochemically inert material such as platinum or graphite ^[12].

1.2.1.2 MASS TRANSPORT

There are three main processes that facilitate the movement of charged particles (or neutral species) in an electrochemical cell to the electrode surface; Diffusion, convection and migration ^[12-13].

Diffusion occurs due to an established concentration gradient, which spontaneously moves the analyte species from areas of high concentration toward areas of lower concentration.

Convection occurs when a force is applied to the solution species, such as mechanical stirring, solution flow, rotation and/or vibration of the electrode.

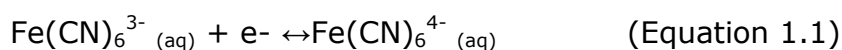
Migration refers to movement of charged particles as a response to an electric field ^[14].

1.2.1.3 ELECTROCHEMICAL EQUILIBRIUM: INTRODUCTION

Electrochemical equilibrium refers to a state of equilibrium at the electrode surface between ions in solution and electrons in the metal electrode. In this study $\text{Fe}(\text{CN})_6^{4-/3-}$ is used to establish an electrochemical equilibrium. When



hexacyanoferrate(II), $K_4Fe(CN)_6$, and potassiumhexacyanoferrate(III) $K_3Fe(CN)_6$, are dissolved in water, a state of equilibrium is reached when the rate at which the $Fe(CN)_6^{4-}$ donates electrons to the metal electrode is equal to the rate at which electrons are released by the electrode to the $Fe(CN)_6^{3-}$ anions (Equation 1.1). The $Fe(CN)_6^{3-}$ obtains an electron and is therefore reduced while the $Fe(CN)_6^{4-}$ loses an electron, and is therefore oxidized .



When equilibrium is reached, the reaction can lie to the right or the left, this indicates that a charge separation has developed at the electrode-solution interface. Thus an electrode potential is established at the metal electrode relative to the solution, this chemical process is generally referred to as a potential determining equilibrium. Other examples where an electrochemical process is capable of forming a potential on the electrode in an aqueous medium include: (i) the hydrogen electrode, (ii) the silver/silver chloride electrode and (iii) the calomel electrode [5].

1.2.1.4 ELECTROCHEMICAL EQUILIBRIUM: ELECTRON TRANSFER AT THE ELECTRODE-SOLUTION INTERFACE

The electrical double layer is essentially an array of charged species and oriented dipoles at the electrode-solution interface. This layer adjacent to the electrode surface can accept or donate electrons to the species present in solution and its composition differs from the bulk solution due to chemical and/or physical changes at the electrode solution interface [5].



The most recognised double layer model was proposed by Helmholtz in 1879, Helmholtz described the electrical double layer as a spatial charge distribution at an electrode/electrolyte interface. He believed it to be a simple capacitor in which a single layer of ions are adsorbed onto the electrode surface and the layer thickness depended on the ion size and the voltage. This was followed by a model proposed by Louis George Gouy and David Chapman. The Gouy-Chapman model focused on the ion distribution in the bulk solution and incorporated a more physical phenomenon in which the distance distribution from the electrode interface was calculated based on various assumptions, such as the presence of thermal fluctuation and consideration of ions as point charges. This model is in accordance with the Boltzmann energy distribution law and together with the Poisson electrostatic law, showed that the potential in the inner layer decreases linearly with the distance from the electrode whereas the diffusion layer has an exponentially decreasing potential.

However the Gouy-Chapman model failed for highly charged double layers. In 1924 the Stern model was developed, it combined the Helmholtz compact layer with a diffuse ion layer. These ions have a finite size and include their solvated shell. These discoveries lead to the establishment and usage of the integrated Gouy-Chapman-Stern model which stated that three imaginary planes are present in an electrical double layer (Figure 1.1); they were described as the inner Helmholtz plane (IHP), outer Helmholtz plane (OHP) and the diffuse or Gouy layer.

The IHP consisted of the adsorbed ions and solvent layer adjacent to the electrode, the OHP consisted of hydrated counter ions electrostatically adsorbed to

the IHP and the Gouy layer consists of the OHP and the remaining counter ions. The Gouy layer is commonly referred to as the bulk portion of the solution.

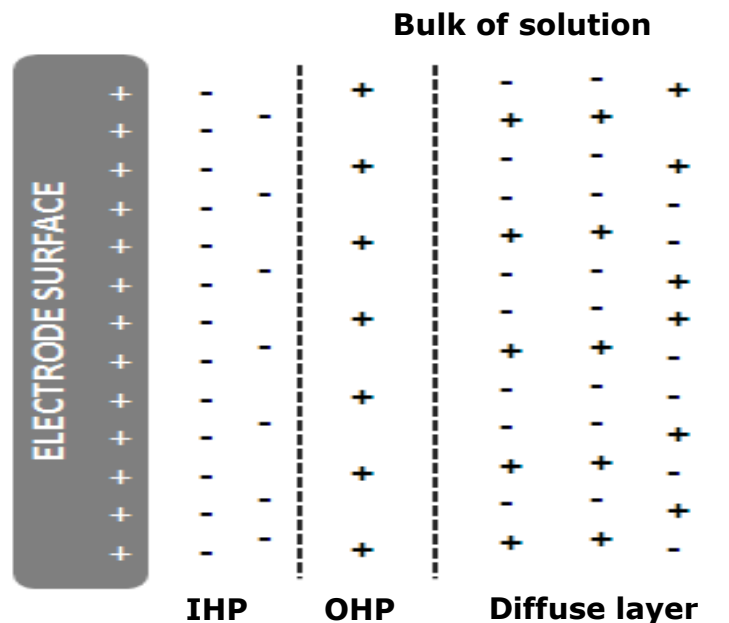


Figure 1. 1 The integrated Gouy-Chapman-Stern model illustrating the three imaginary planes that are present in an electrical double layer

The electrodes involved in the electrical double layer can donate or accept electrons from the layer of species adjacent to the electrode surface. When a voltage is applied to the system, there is a momentary surge of current at the IHP onto the electrode surface, which rapidly decays to zero if no reactive species is present. This is the charging current that creates an excess or deficiency of negative charges at the surface and significantly affects the OHP. So when electrons interact at this electrical layer, two processes are possible; the electron can remain at the electrode surface thereby increasing the charge on the double layer, alternatively the electron will be involved in a chemical reaction involving the



electroactive species. These are termed non-faradaic and faradaic processes respectively.

1.2.1.5 FARADAIC AND NON-FARADAIC PROCESSES

Faradaic current is a current response to the oxidation or reduction of an analyte species at the electrode-solution interface. This current is a direct measurement of the rate of the electrochemical redox reaction. For a thermodynamically controlled reversible process the applied potential of the electrode is given by the well known Nernst Equation, Equation 1.2:

$$E = E^{\circ} + \frac{2.303RT}{nF} \log \frac{C_{oxi}}{C_{red}} \quad (\text{Equation 1.2})$$

Where, E° = standard potential of the redox couple

R = universal gas constant (8.31 J K⁻¹ mol)

T = temperature (K)

n = number of electrons transferred

F = Faradays constant (9.64x 10⁴ C mol⁻¹)

C_{ox} = concentration of the oxidized species

C_{red} = concentration of the reduced species.

Non-faradaic current is a current response that does not involve the transfer of electrons across the electrode-solution interface, these electrons stay at the electrode surface and increase the charge on the electrode surface which enhances



the polarization of the electrochemical system. Thus non-faradaic current is due to the capacitive nature of the electrode interface.

The capacitance, C , of the electrical double layer can be calculated using Equation 1.3:

$$C = \frac{q}{E} \quad (\text{Equation 1.3})$$

Where q and E are the charge and potential respectively.

1.2.1.6 CLASSIFICATION OF ELECTROCHEMICAL TECHNIQUES

Electrochemical techniques can be classified as either a bulk or interfacial technique. Bulk methods are based on the bulk portion of the solution and interfacial methods refer to the reactions occurring at the interface between the electrode surface and the thin layer of solution adjacent to that surface ^[15].

1.2.2 VOLTAMMETRY

1.2.2.1 CYCLIC VOLTAMMETRY

Cyclic voltammetry is an extensively used electrochemical technique that is used to investigate the reversibility and kinetics of electrochemical reactions ^[16]. The potential of an electrode is scanned linearly from an initial potential to a final potential and then back to the initial potential. The current flowing through the working electrode is as a result of a set applied potential, the current is recorded and a plot of the current versus applied potential is produced (Figure 1.2).

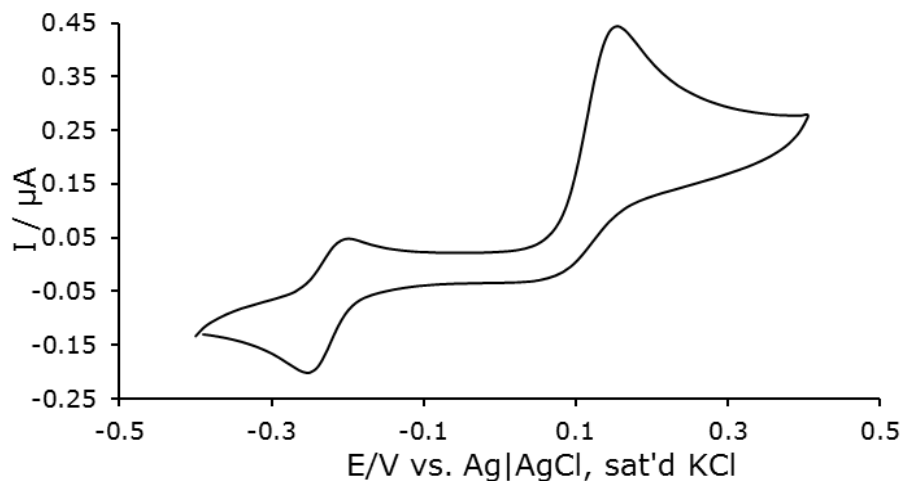


Figure 1. 2 Typical Cyclic Voltammogram for a reversible process

As the potential moves forward toward more positive values, an anodic current flows and an anodic peak appears (I_{pa}). In the reverse direction, the potential moves towards more negative values and a cathodic current flows, this results in the cathodic peak (I_{pc}). An anodic and cathodic current will promote the oxidation and reduction processes respectively. The potential at which the current peaks occur is known as the peak potential (E_p), at this point the redox species has depleted at the electrode surface and the current is diffusion limited. The magnitude of the faradaic current peaks (I_{pa} and I_{pc}) is indicative of the rate of electron transfer between the electrode and redox species.

Cyclic voltammograms can indicate if a reaction is reversible, quasi-reversible or non-reversible.



REVERSIBLE PROCESS

A reversible process is defined by a rapid electron transfer process in which the electroactive species in the forward scan and reverse scan are in equilibrium. At this equilibrium the species are stable and so the magnitudes of I_{pc} and I_{pa} are the same and proportional to the solution species concentration. The potential difference (ΔE) is the difference between E_{pa} and E_{pc} , it is independent of the scan rate (ν) however due to solution resistance (R_s) between the reference and working electrode, ΔE can increase slightly as the ν increases.

For a reversibly reaction, if only one electron ($n=1$) is transferred during the reaction at 298 K, the difference between the E_{pa} and E_{pc} will be between 57 mV and 60 mV, however if more than one electron ($n>1$) is transferred in the system then $\Delta E = 60-100$ mV ^[17-18]. Reversibility is proportional to the stability of an electroactive species as a reversible process will form a stable product that will remain near the electrode surface. Unstable species react as they are formed and this affects the current in the reverse scan by distorting the reverse current peak to have larger potential differences or asymmetric current peaks. These characteristics are indicative of an irreversible process.

The magnitude of the current peak is given by the Randles-Sevcik Equation ^[19-20]
(Equation 1.4):

$$I_p = (2.69 \times 10^5) n^{3/2} AC(D\nu)^{1/2} \quad (\text{Equation 1.4})$$

Where, I_p = peak current

n = number of electrons transferred



A = electrode area (cm^2)

C = concentration ($\text{mol}\cdot\text{cm}^{-3}$)

D = diffusion coefficient (cm^2s^{-1})

ν = scan rate (Vs^{-1})

Linear plots of I_p vs. $\nu^{1/2}$ are indicative of planar mass diffusion to the electrode surface [21]. These systems also have the ratio of the I_{pa} and I_{pc} equal to 1, deviations from this ratio indicate that a competing chemical reaction has occurred. This competing reaction can result in the formation of unwanted species which decreases the current from the cathodic reduction process, therefore $I_{pa} > I_{pc}$ and this indicates the system is not reversible.

The potential, at which the concentration of the oxidized and reduced species in the solution is equal, is referred to as the half wave potential. This value is given by Equation 1.5.

$$E_{1/2} = \frac{(E_{pa} + E_{pc})}{2} \quad (\text{Equation 1.5})$$

The subscript 1/2 indicates that the potential is obtained at approximately half the height of the cathodic and anodic peaks. E_{pa} and E_{pc} are the anodic and cathodic peak potentials respectively. The number of electrons transferred during the reaction and the peak potential difference (ΔE_p) can be calculated using the Equation below;

$$\Delta E_p = E_{pa} - E_{pc} = 2.303 \frac{RT}{nF} \quad (\text{Equation 1.6})$$



ΔE_p is independent of the scan rate and at 25°C Equation 1.6 can be simplified to Equation 1.7:

$$\Delta E_p = 2.303 \frac{RT}{nF} = \frac{0.059V}{n} \quad (\text{Equation 1.7})$$

Where all symbols are as defined above.

IRREVERSIBLE PROCESS

Electrochemical irreversibility is caused by slow electron exchange of a particular species with the working electrode. The peak current, I_p for an irreversible process is given by Equation 1.8:

$$I_p = (2.99 \times 10^5) n [(1 - \alpha)n]^{1/2} A c (D\nu)^{1/2} \quad (\text{Equation 1.8})$$

Where α is the coefficient of electron transfer, and the other variables are defined above. In an irreversible system, E_p and $E_{1/2}$ differ by $0.048/\alpha n$, this is calculated using Equation 1.9:

$$\Delta E_p = E^\circ - \frac{RT}{\alpha nF} [0.78 - \ln \frac{k}{D^{1/2}} \ln (\frac{\alpha nF}{RT})^{1/2}] \quad (\text{Equation 1.9})$$

Where all symbols are as defined above.

QUASI-REVERSIBLE PROCESS

A process is quasi-reversible if the rate of electron transfer and the rate of mass transport do not maintain the nernst equilibrium at the electrode surface. Quasi-reversible processes do not have a linear relationship between I_p and $\nu^{1/2}$ and $\Delta E_p > 0.058/n$ V increases proportionally to the scan rate. A quasi-reversible process is characterized as increasing ΔE_p according to the increase in scan rate ($\Delta E_p = f(\nu)$). A quasi-reversible reaction can possibly change to a reversible reaction by



decreasing the scan rate as this may allow more time for the surface concentrations to adjust to the changing potential [22]. The table below summarizes the differences between reversible, irreversible and quasi-reversible processes.

Table 1. 1 Classification criteria for reversible, irreversible and quasi-reversible cyclic voltammetric processes

	Reversible	Irreversible	Quasi-reversible
E_p	Independent of ν	Shifts cathodically by 30/ αn mV for a 10-fold increase in ν	Shifts with ν
$E_{pc} - E_{pa}$	0.058/ n V at 25°C and independent of ν	-	Approx. 60/ n mV at low ν , increases at ν increases
$I_p/\nu^{1/2}$	Constant	Constant	Virtually independent of ν
I_{pa}/I_{pc}	Equals 1, independent of ν	No reverse current	Equals 1 only for $\alpha=0.5$

1.2.2.2 CHRONOAMPEROMETRY

Chronoamperometry is an amperometric method where the solution species undergoes a redox reaction by stepping the potential of the working electrode from an initial electrode potential to the first stepped potential. In a single potential experiment, the potential is held for a set time while the resulting faradic current at the electrode is monitored as a function of time. In a double potential step experiment, the potential is stepped again after the first step time and then changed to the second step potential, it is then held at this value for the second step time.



The faradaic current at any time after the application of the first potential step will obey the Cottrell Equation (Equation 1.10).

$$I = nFD^{1/2}CA\pi^{-1/2}t^{-1/2} \quad (\text{Equation 1.10})$$

A plot of I vs. $t^{-1/2}$ is a Cottrell plot; it defines the current time dependence for linear diffusion control in which the resulting slope is an indication of the diffusion coefficient (D).

The catalytic rate constants (k) at intermediate times of the measurement can be determined using the following Equation:

$$\frac{I_{cat}}{I_L} = \pi^{1/2} (k C_o t)^{1/2} \quad (\text{Equation 1.11})$$

I_{cat} and I_L are the currents of the electrode in the presence and absence of the analyte respectively. C_o is the bulk concentration of the analyte. All other symbols are defined above. The catalytic rate constant can be determined from the slope of the plot of I_{ca}/I_L versus $t^{1/2}$.

1.2.2.2 GALVANOSTATIC MEASUREMENTS

Galvanostatic measurements are a potentiometric technique that describes materials ability to charge and discharge current. If the current induces a fast, faradaic, redox reaction then the material has pseudocapacitive abilities however if it involves non-faradaic current separating the charges at the double layer then it is called an electrochemical double layer capacitor (EDLC) [23-24].

1.2.2.3 ELECTROCATALYSIS

Electrocatalysts increase the rate of chemical reactivity without being consumed in the process, their contribution can be at the electrochemical interfaces or can be the electrode surface itself. An electrocatalyst can initiate a homogeneous or heterogeneous catalytic effect. Heterogeneous catalysis involves various consecutive reactions that are in different phases whereas homogeneous catalysis involves reactions that have the reactive and resulting products in the same phases.

According to Figure 1.3, the catalyst is first oxidized. The electron deficient catalyst then reacts with the analyte which leads to the oxidation of the analyte and the regeneration of the catalyst. These electrocatalysts assist in transferring electrons between the electrode and reactants, and/or facilitate an intermediate chemical transformation [25].

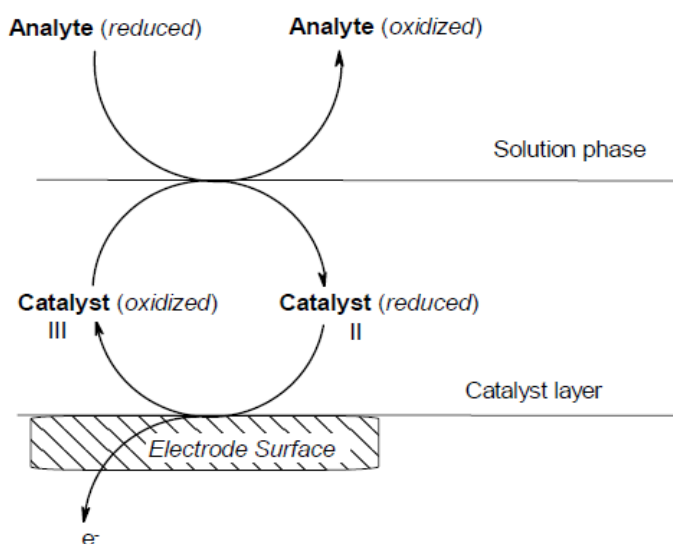


Figure 1. 3 Schematic diagram of the process of electrocatalysis [15]



1.2.2.4 ELECTROCHEMICAL IMPEDANCE SPECTROSCOPY

Electrochemical impedance spectroscopy (EIS) is an important technique used for investigating electrochemical properties of modified electrodes and their systems. One of the most significant applications is its ability to describe the kinetic mechanisms of the various forms of mass transfer as it measures the ability of a circuit to resist the flow of electrical current. But unlike a typical resistance which is based on an ideal resistor; it's not limited by one circuit element.

A sinusoidal potential is applied, $v(t)$, to an electrochemical cell and the resulting current $I(t)$, measured through the cell. The resulting current and applied potential are represented as a function of time, the time dependence of this impedance can reveal underlying chemical reactions thus revealing significant internal dynamic processes [26].

Generally the cell is excited with a sinusoidal potential and the response to the potential is an AC current signal. Such data gives both physical and chemical properties of the material and thus the impedance (Z) can be defined by the Equation below

$$Z = \frac{v(t)}{I(t)} \quad (\text{Equation 1.12})$$

where $v(t)$ is the sinusoidal applied potential at time (t) according to $v(t) = v_0 \sin(\omega t)$ where v_0 is the max potential amplitude and ω is the radial frequency (in rads^{-1}) and can be related to the frequency according to $\omega = 2\pi f$. At the same frequency of the applied sinusoidal potential the current response $I(t)$ is



sinusoidal with a phase shift, $I(t) = I_0 \sin(\omega t + \theta)$, where I_0 is the maximum current applied and θ represents the phase shift by which the voltage lags the current ^[27].

As a vector, the Z has direction, which is described by the phase angle (Φ), and magnitude, which is described by the ratio of the voltage amplitude to the current amplitude. This can be described using the following Equation:

$$Z = Z' + jZ'' = Z_{\text{real}} + Z_{\text{imaginary}} \quad (\text{Equation 1.13})$$

where Z' and Z'' are the real and imaginary components of the impedance value respectively and j is a complex number ^[28].

IMPEDANCE DATA INTERPRETATION

The interpretation of electrochemical data is simplified by using circuit equivalent analogs, these circuits consisted of simple components such as resistors and capacitors. The resistance in the circuit represents the electrical conductivity of the electrolyte and the constant phase element (CPE) stemming from the excess charge at the electrode-solution interface. The most used circuit to fit EIS data is the Randles equivalent circuit. The Randles equivalent circuit shows the solution or electrolyte resistance, R_s , connected in series to a combination of charge transfer resistors in parallel, R_{CT} , and the CPE.

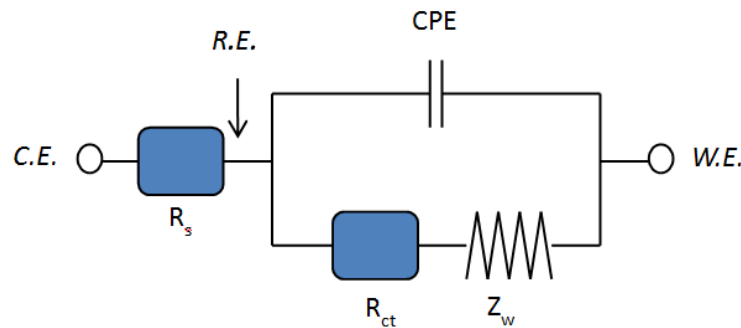


Figure 1. 4 The Randles equivalent circuit ^[15]

The conditions of the transport and diffusion of the electroactive species is a significant component as it affects the reaction rate. The impedance supplied by this mass transfer is called the Warburg Impedance (Z_w) and is connected in series to the charge transfer resistor. Impedance data can be graphically represented on a Nyquist plot (Figure 1.5), which plots the Imaginary Z'' against real Z' component of the impedance data. Typically each plot gives rise to a semicircle, from which the component R_s and C_d values may be extracted. The charge transfer resistance is proportional to the diameter of the semicircle at high frequencies and a straight line at low frequencies.

On an Nyquist plot the impedance can be represented as a vector arrow of length $|Z|$ and the angle between the vector and X-axis is the phase angle (Φ).

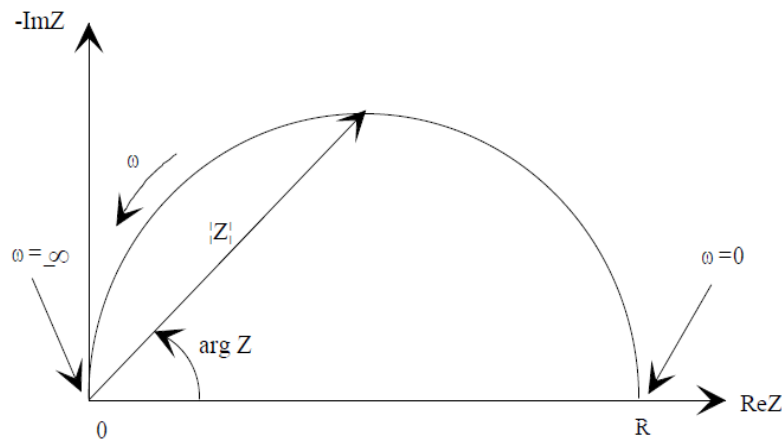


Figure 1.5 Typical EIS Nyquist plot ^[1]

Another popular representation method is the bode plot. The impedance is plotted with the log frequency on the x-axis and both the absolute values of the Impedance ($|z| = z_0$) and the phase- shift on the y-axis. The significance of these plots is that they show the frequency at which the data point was recorded.

Impedance spectroscopy is a non-destructive technique and offers many advantages as it describes the electrochemical reactions in fuel cells, batteries or any other electrochemical process. The most valuable properties of EIS are;

- I. low amplitude sinusoidal voltages to maintain the system at equilibrium.
- II. Determination of the Ohmic resistance, capacitance, film conductivity and charge transfers at the electrode-solution interface.
- III. Accurate, adaptable, repeatable and rapid measurements.
- IV. Characterisation of interfacial properties with/without redox reactions.



1.3 MODIFIED ELECTRODES

An electrode made of conducting or semiconducting material, which is coated with a film of a chemical modifier, is termed a chemically modified electrode. These films promote reactions due to charge transfers or chemical/electrochemical potential differences. Modified films can significantly improve the electrocatalytic properties of substrates, decrease the overpotential and improve the stability and reproducibility of the electrode response ^[29].

1.3.1 METHODS OF MODIFYING ELECTRODE SURFACES

There are various chemical techniques to apply the modification material onto the electrode surface, a few of these techniques are mentioned below.

Covalent: Electrodes can be modified by covalently attaching a species to the surface of the electrode or to an adjacent layer. These covalent bonds are very strong and layer upon layer of modification can produce electrodes of great sensitivity.

Drop-dry coating: The material is drop dried onto the electrode surface.

Electro-polymerisation: The electrode is immersed in a polymer and a potential is swept across the system, this initiates the formation of layers of the electro-polymerized material on the electrode surface ^[30].

Chemisorption: Chemisorption differs from general adsorption, as chemisorption is driven by a chemical reaction that occurs at the electrode surface and produces a new chemical species for example metallic oxidation ^[31].



1.3.2 SELF-ASSEMBLED MONOLAYERS

Self-assembled monolayers (SAMs) are created from molecules that are classified based on their potential to bind favourably via a specific interaction to a particular surface thus forming a stable monolayer that remains intact even after the substrate is removed from the solution. The transport process of the adsorbate to the substrate can be solely diffusion, adsorption controlled or a mix between the two processes.

Techniques such as X-ray photoelectron spectroscopy (XPS), Fourier transformation infrared spectroscopy (FTIR) and Atomic force microscopy (AFM) have been used to understand the mechanism involved in the formation of SAMs. Yamada & Uosaki performed various in situ STM experiments in heptane solutions, they monitored the growth of an alkylthiol onto a gold surface and observed three steps involved in SAM growth ^[32-33]. Further publications by Šustrová et al., have supported this 3 step process ^[34]. The initial step is the immediate adsorption of the adsorbent onto the substrate to form strong covalent bonds, it takes approximately 10 minutes for the initial adsorption to occur in which isolated adsorbed molecules are distributed unevenly in a disordered and random manner ^[35]. The adsorbent substituents then begin to reorient themselves based on their initial random orientation and the surrounding intermolecular bonds with neighbouring constituents. The final step and slowest step in the monolayer formation is the adherence of all constituents, away from their disorder and into a uniform and tightly packed monolayer. The monolayer is packed into an arrangement that minimizes the free energy of the layer and adopts a conformation that allows



extensive van der waals forces and hydrogen bonding between adjacent molecules [36].

The addition of a long chain alkylthiol (>8) has an approximate adsorption time of 12-24 hours, in which it produces tightly packed and order SAMs [37-38]. These tightly packed monolayer are relevant mostly to systems in which further attachments are added, such as the bonding of carbon nanotubes [39]. Recent studies have indicated that electrostatic interactions are sufficient in the preparation of modified surfaces [40], as they produce a net polarity on the electrode surface [41-42].

Utilization of the ideal parameters can significantly optimize SAMs and ensure greater reproducibility. The solvent can be polar or nonpolar and generally is best at room temperature as it improves the kinetics and reduces inconsistencies in the layer. Extensive cleaning of the substrate surface prior to use is essential as contaminants can result in monolayer defects, other defects can generally be attributed to thermodynamic instability. Typically a lower concentration of solution would require a higher adsorption time. Other variables such as chain length [43], thiol constituents, substrate properties and intermolecular bonds are also significant factors.

1.3.3 LAYER BY LAYER SELF-ASSEMBLED MONOLAYERS

The technique of layer-by-layer self assembly (LBL) is based on the fundamental principles of SAMs however incorporates more than one layer. The synergistic effect of the modification material and the electrode allow a covalent or electrostatic interaction to occur and a modified layer to form. It is a controlled coordination or



stepwise self assembly strategy. Each monolayer is added by layering alternating materials containing complementary functional groups to form integrated, well-organized arrangements of multilayered films on an electrode surface.

1.4 NANOPARTICLES

GENERAL OVERVIEW

Nanoparticles are of great scientific interests as due to their small size, exhibit unique chemical, physical and electronic properties that are different from those of their bulk form. The synthesis of nanoparticles is a field that combines the conventional inorganic cluster chemistry and the classical colloidal chemistry ^[44]. For over a century, metallic nanoparticles have interested scientist. These materials can be synthesised and modified with various chemical functional groups which enhance their applications. Possible modification includes conjugation with antibodies, ligands or complimentary chemical compounds.

1.4.1 GOLD NANOPARTICLES

HISTORICAL PERSPECTIVE

Colloidal gold, also known as gold nanoparticles, is a suspension (or colloid) of nanometre-sized particles of gold, a term coined in 1974 by Noroi Taniguchi ^[45]. The history of these colloidal solutions dates back to Roman times when they were used to stain glass for decorative purposes. Colloidal gold was used to stain glass intense shades of red or mauve in which the resulting colour depended on the concentration of gold ^[46]. A significant, iridescent glassware created was the Lycurgus cup, a glass that contained gold-copper alloyed nanoparticles and



changed colour when light shone through it. The glass looked green in reflected light but red when light passes through it ^[47].

In the seventeenth century, the first 'ruby glass' was made by Andreus Cassius and named the "*Purple of Cassius*" due to its rich colour. Many famous chemists in the eighteenth and nineteenth centuries attempted to understand the nature of this material but none were completely successful. In 1857 Faraday reported the formation of a deep red gold solution that formed upon the reduction of aqueous chloroaurate (AuCl_4); he claimed the colour was indicative of the minute size of the gold nanoparticles. However it was Richard Zsigmondey who discovered that the gold was in a colloidal form, his further work on colloidal gold nanoparticles resulted in Zsigmondey being awarded the Nobel Prize in 1925 ^[48].

The understanding of colloidal gold nanoparticles has significantly developed since these discoveries, the synthesis of gold nanospheres, nanorods, nanoclusters, nanostars and nanocubes are now possible, each with their own unique spectral and structural properties ^[3].

SYNTHESIS AND STRUCTURE

One of the main methods of synthesizing gold nanoparticles is the innovative two-phase Brust-Schiffrin method, in which AuCl_4 is reduced by sodium borohydride in a toluene solution containing stabilizing thiols ^[49]. Another reliable method is the older Turkevich synthesis methodology ^[50], where gold salt is boiled together with citrate to get 10-15 nm water-soluble particles. UV initiated particle growth is another newer technique which aims to improve the size distribution and spherical shape of larger sized gold nanoparticles, potentially between 9-120 nm ^[51-52].



Recently significant progress has been made in synthesizing non-spherical gold nanoparticles such as nanorods using seed-mediated growth. Other synthetic methods for gold nanorods include the template method and electrochemical methods ^[53-54].

The size, shape and dispersity of gold nanoparticles are controlled by adjusting the experimental conditions and reagents. To manipulate the growth of gold nanoparticles beyond their spherical growth, additives are used which bind to the nanoparticle surface. This coordination chemistry between a surfactant, ligand, adsorbate, chelating agents or polymers and the nanoparticle surface is of fundamental importance in achieving shape control ^[55]. Since gold preferentially reacts with sulphur donors, rather than oxygen and nitrogen donors, gold nanoparticles can be substantially stabilised by thiolate ligands as the strong interaction between the sulphur of the thiolate ligands allows a protective shell to form around the nanoparticle ^[56]. This decreases the coagulation of the particles and increases the stability, electronic, optical and catalytic functions ^[57-58].

PROPERTIES

Gold nanoparticles have excellent catalytic abilities, optical activity, biocompatibility, photoluminescent and electrical properties. Spherical gold nanoparticles are optically active at absorb lights of 520 nm whereas gold nanorods are optically active at two distinct absorbance bands. Accordingly the bands are due to the transverse and the longitudinal oscillations that take place along the width and length respectively. The wavelengths of these oscillations are typically 250 nm for the transverse region and 520 nm for the terminal, spherical region. The optical



activities of gold nanorods are dependent on the length-to-diameter ratio of the nanorods ^[59].

APPLICATION

Due to their remarkable properties, the applications of gold nanoparticles stretch from mechanical devices to medicinal applications. Gold nanoparticles have been used widely in optical devices, electrophoresis, optoelectronic devices, fluorescence, catalysis, biochemistry, drug delivery and sensors ^[60].

This work focuses on the combination of nanoparticles with MWCNT for enhanced electrochemical sensor development. Nanocomposites of MWCNT and nanoparticles have great potential in detection of trace analyte quantities. This is due to the emerging property that results from the combined effect of the materials that is not present in their individual states ^[61].

1.4.2 CARBON NANOTUBES

HISTORICAL PERSPECTIVE

As a result of the wars and revolutions experienced by Europe and the USA, many scientific discoveries may not have been acknowledged ^[62]. This has resulted in great difficulty in determining the original founders of certain key international discoveries. Carbon nanotubes (CNT) are one such example.

In 1952 Russian scientists, Radushkevich and Lukyanovich, published a paper in *The Soviet Journal of Physical Chemistry*, in which they described hollow graphite carbon fibres ^[63]. This was the first mention of “carbon nanotubes” but as a result of the Cold War the research was not recognised internationally. A few decades



later, subsequent to Iijima's publication in Nature ^[64], the discovery of CNTs were regarded as one of the most influential discoveries that significantly changed the scientific world. However Iijima's "rediscovery" came at the back of several other breakthroughs. In 1960, Bollmann and Spreadborough documented the frictional properties that exist from the rolling of sheets of graphene in nature ^[65]. This was followed by Wiled and Abrahamson documenting the growth of small fibres on graphite and carbon anodes in 1978 ^[66]. Then in 1976, the original synthetic method for CNT was developed by Oberlin et al., they reported Chemical Vapour Deposition (CVD) growth of carbon fibres ^[67] however earlier mentions of synthetic methods date back to 1889 in which thermal decomposition of gaseous hydrocarbons were used ^[68]. Further incorrect accreditation occurred in 1985, when it was believed Smalley et al., discovered fullerene molecules when in fact 5 year prior, Iijima had identified the first fullerene molecule using an electron transmission microscope ^[69-70].

In 1981, a group of Soviet scientists published the results of chemical and structural characterisation of carbon nanoparticles produced by a thermocatalytical disproportionation of carbon monoxide in a Russian local journal. Using TEM and X-ray diffraction microscopy images, the authors suggested that their "carbon multi-layer tubular crystals" were formed by rolling graphene layers into cylinders ^[71]. However it was Iijima's international report in 1991 that impacted our knowledge of CNT by his discovery of MWCNT in the soot of arc discharges ^[31]. He then development a procedure in synthesizing bulk CNT using the arc discharge method as well as contributing to the extensive understanding of the physical and electronic properties of CNTs ^[72]. In 1992 the USA released the first theoretical predictions of

the electronic properties of single-walled carbon nanotubes (SWCNT) before its actual discovery in 1993 ^[73]. The discovery was made by two independent groups, Bethune ^[74] and Iijima ^[39] respectively. Iijima and Iichashi were credited for the discovery of SWCNT having submitted their manuscripts a month before that of the US team. According to Iijima, the formation of the first SWCNT was due to a failed attempt in the production of MWCNT containing transition metals.

In 1996 Smalley and co-workers introduced a new technique for the synthesis of SWCNT, known as dual-laser ablation ^[75]. A few years later, a new synthetic method known as ball milling and subsequent annealing of CNTs was used to produce more MWCNT than SWCNT ^[76]. From the discoveries made, CNT's can be summarised into the following; SWCNT, MWCNT and the more recent, double-walled carbon nanotube (DWCNT) (Figure 1.6) ^[77]. The DWCNT are composed of exactly two single-walled carbon nanotubes whereas MWCNT contain multiple concentric layers of hollow graphene cylinders ^[78]. The MWCNT are the most stable and thus are abundant in nature ^[79-80].

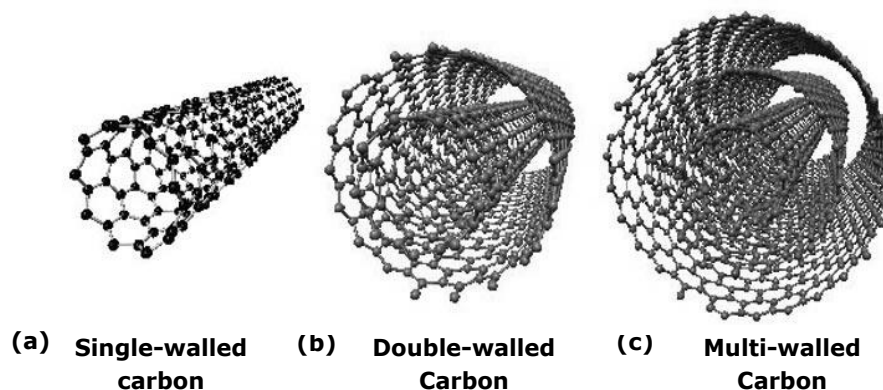


Figure 1. 6 Illustration of (a) Single-walled carbon nanotubes (b) double-walled carbon nanotubes and (c) Multi-walled carbon nanotubes ^[154]

SYNTHESIS AND STRUCTURE

CNTs are hollow tubes composed of carbon atoms arranged in a hexagonal lattice. The nature of bonding in CNTs is described by applied quantum chemistry, specifically orbital hybridization. Each carbon atom is covalently bonded to three neighbouring carbons via sp^2 molecular orbitals ^[81]. The fourth valence electron, in the p_z orbital, hybridizes with all the other p_z orbitals to form a delocalized π -bond. The formation of high strength CNT fibres can be credited to these strong chemical bonds as this bonding structure is stronger than the sp^3 bonds found in diamonds. This provides the molecules with its unique strength ^[82]. Under high pressure, nanotubes can change their sp^2 bonds for sp^3 bonds, this causes them to merge together and allows CNT to form strong, excessively long wires through high-pressure nanotube linking ^[83].

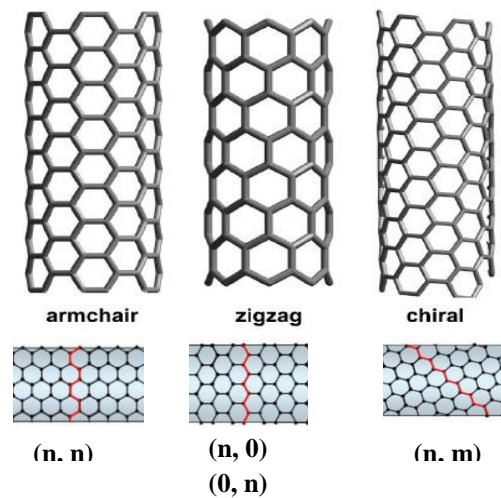


Figure 1. 7 Illustrating the various CNT structures ^[86]



The structure of a CNT can be visualised by wrapping a one-atom-thick layer of graphite into a seamless cylinder. The manner in which the graphene sheet wraps, can be represented by a pair of indices (n, m) called the chiral vector. Different relationships between n and m result in different structures. There are 3 main types, the armchair, zigzag and chiral structure (Figure 1.7). When the chiral vector $n = m$ and chiral angle equals to 30° , it produces the metallic arm chair structure. The zigzag structure has an $n = 0$ or $m = 0$ and chiral angle equal to 0° whereas the chiral structure has $n \neq 0, m \neq 0$ and the chiral angles is between 0° - 30° . The manner in which the graphene is rolled, determines the conductivity of the CNT, it can be classified as metallic, semi-metallic or semi-conducting ^[84-85].

The length of MWCNT range from a few tens of nanometres to several micrometers and have an outer diameter of between 2.5-30 nm ^[86]. These factors significantly influence the electrical conductivity, thermal conductivity, density and lattice structure. However the conductivity in MWCNT is quite complex as inter-wall reactions can cause the non-uniform redistribution of current ^[87]. There are two models which can be used to describe the structures of MWCNT. The Russian Doll and Parchment models. The Russian Doll model involves sheets of graphite arranged in concentric cylinders whereas the Parchment model is a single sheet of graphite rolled around itself ^[52]. SWCNT have an inner diameter of 4 nm and the inner tubes are curled and looped rather than straight. The small diameter of SWCNT have an important effect on their mechanical properties and are associated with high flexibility and strength stiffness, a property that is absent in graphite fibres ^[88].



Functionalisation of CNT results in enhanced solubility and sensitivity. Since the “rediscovery” in 1991, these CNTs have been at the forefront of development due to their role in biological, environmental and chemical application. The fundamental challenge in functionalising the CNT is the removal of the metallic catalyst present in the raw commercial form and further severing of the long rope like texture into shorter pieces [89]. It has been deemed a necessary pathway to derivatise these materials as modification results in the enhanced ability of CNT as the exposed carboxylated ends can form intermolecular bonds with conductive material.

PROPERTIES

CNTs have attracted particular interest due to their unique structure, nanosized scale and physico-chemical properties.

They have high thermal conductivity, elasticity, conductivity, electronic and vibrational properties. CNTs are one of the stiffest and strongest fibres known, and have remarkable electronic properties. The intense mechanical properties are based on the strength of the quasi-one-dimensional sp^2 -bonded structure [44]. These carbon-carbon bonds give CNTs intense strength as nanowires. These CNTs possess a high surface area with an excellent surface-to-area ratio and can store ions [47- 52].

APPLICATIONS

Recent applications of CNTs are found in electronics, catalysis and biomedical research. Among these applications, significant interest and development has been shown in ceramics, fuel cells, hydrogen energy storage, rechargeable lithium



batteries, photodetectors, solar cells, steal coatings, waste water detection and supercapacitors. Numerous neurodegenerative diseases are caused by abnormal processes and concentrations in neurotransmitter-based signaling. Detection of neurotransmitters by nanoparticle sensors began in 1996, where MWCNT modified with glassy carbon electrodes were used to detect dopamine ^[90]. Then in 2001, Li and co-workers catalysed the electrochemical reaction of dopamine, epinephrine and ascorbic acid using carboxyl terminated single-walled carbon nanotubes on glassy carbon electrode ^[91].

Sensors enhanced by chitosan, hydrogen peroxide, insulin, nucleic acids , aluminium oxide membranes, Silicia acid tetracthyl ester, cysteamine and serotonin had been investigate to detect for neurotransmitters such as cysteine ^[92], tyramine ^[93], epinephrine, ascorbic acid and dopamine ^[43-46]. These modification materials are applied to the gold electrodes using different methods such as polymerisation, self-assembly or the layer-by-layer method. The performances of these electrodes were found to be superior to other methods of detection due to cost, time and low limits of detection. In terms of promoting electron-transfer and improving reversibility these electrochemical sensors produced results that resulted in an emerging area of research based on further modification of CNTs with metallophthalocyanine (MPc) and nano-MPc complexes.

1.4.3 PHTHALOCYANINE

HISTORICAL PERSPECTIVE

In 1907, Braun and Tchermiac failed in their attempt to produce o-cyanobenzamide by dehydrating phthalamide using acetic anhydride. Instead they obtained a small



quantity of a bright bluish compound, this compound was thereafter recognised as metal-free phthalocyanine ^[94]. Unfortunately, the scientists did not recognize the impact of their discovery of this unique complex with extraordinary properties. 20 years later another accidental synthesis of the phthalocyanine complex occurred. Swiss Chemists Von der Weid and de Diesbach tried to synthesize phthalonitrile from o-dibromobenzene and cuprous cyanide. However a deep blue copper complex was formed, essentially a process called cyclotetramerizing occurred in which the phthalonitrile changes in the presence of cuprous bromide to form a semi-bromo copper phthalocyanine and other copper phthalocyanine derivatives ^[95].

Thereafter Scottish Dyes Ltd. in a reaction of phthalic anhydride and urea failed to produce their desired product, phthalimide, and instead formed a significant mass of a bluish-green coloured product. In their investigation of this occurrence, a crack was discovered on the inner glass lining of the reactor resulting in a part of the reactant inside the vessel being exposed to the outer steel lining. A blue impurity formed when the reaction mass containing phthalic anhydride, phthalimide and ammonia interacted with the iron. The conditions were replicated in the laboratory and the unwanted impurity, iron phthalocyanine was successfully synthesized by reacting phthalic anhydride, ammonia and iron filings ^[96]. In 1929, Scottish Dyes Ltd obtained a patent for the preparation of phthalocyanine complex from phthalic anhydride, a metal salt and ammonia. After further studies of the complex, the empirical formula was revealed to be $C_{32}H_{16}N_8M$ in which M was a transition metal ^[97].



In 1934, Sir Reginald Linstead and co-workers suggested that the phthalocyanine complex was a macro cyclic structure and named it phthalocyanine [98]. This name stemmed from the terms phthalo from naphtha meaning oil and cyanine meaning blue. This structure was confirmed by M. Robertson. Using X-ray crystallographic analysis, Robertson showed that the molecule was in fact a planar macrocyclic structure [99-100].

STRUCTURE AND SYNTHESIS

Phthalocyanine complexes are planar, macrocyclic compounds consisting of four isoindole units linked together by nitrogen atoms [101]. The system is structurally similar to that of the aza-[18]-annulene series, commonly known as porphine. The molecule is an 18 π -e⁻ conjugated structure thus has exceptional stability. The excellent stability of these compounds can be attributed to the molecule symmetry as well as the lack of any dipole moment [102]. The metal atom located in the central cavity of the complex is well protected within the molecule. This inner metal atom is covalently bonded to two nitrogen atoms in the porphine ring and has a co-ordinate linkage with two other nitrogen atoms of the same ring though the lone pairs on the nitrogen atoms (Figure 1.8a).

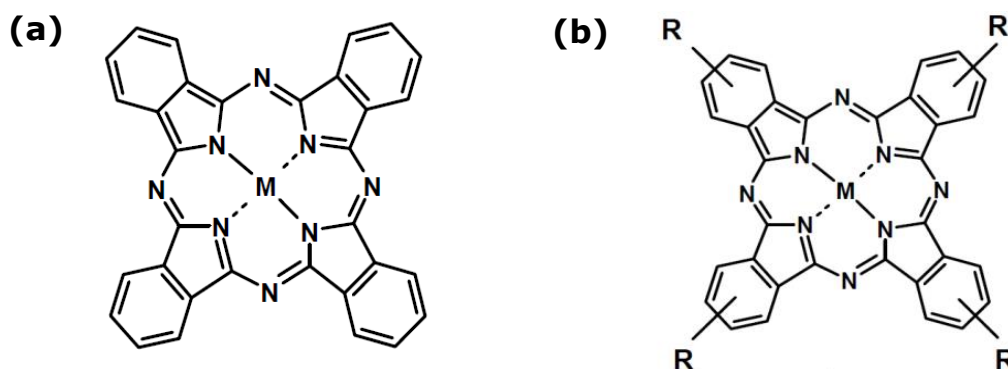


Figure 1. 8 Illustration of a) the phthalocyanine complex (M= transition metals such as Cu, Co Ni etc.) and b) the phthalocyanine complex with R-Group substituent's.

Exterior substitution can be made on to the phthalocyanine ring. Replacement of the isoindole unit with various other heterocyclic rings has been reported in which the phthalocyanine macrocycle can complex with various different elements. The strength of the metal attachment to the inner cavity is dependent on the metal, for example the Cu^{2+} ion binds strongly and can only be removed by the complete destruction of the outer structure whereas metal complexes of Li^+ and Mg^{2+} ions are unstable, and can be easily removed with dilute acids. In such cases, metal-free phthalocyanine complexes are produced that are turquoise blue.

According to Somashekarappa et al, the addition of chlorine to the phthalocyanine complex changes the colour from blue to a lighter green and produces a final product with excellent light fastness, heat stability and resistance to acids, and alkalines [103-104]. The Somashekarappa group has well documented the synthesis and structures of various metallophthalocyanine complexes and have reported that the physico-chemical properties of various metallophthalocyanine



complexes depend primarily on the number and positions of substituents on the molecule (Figure 1.8b) ^[109-105].

The synthetic procedure of the phthalocyanine has significantly developed since their first production in the early 1990's using the traditional ball and milling process ^[106-107]. These particles were up to 100 nm and showed unique absorptive properties. Following decades involved the formation of oxotitanium phthalocyanine nanosized particles dispersed in resin and oxovanadium phthalocyanine ^[108-109]. The preparation of such particles essentially required the use of precursors such as phthalic anhydride, diiminoisoindoline, phthalonitrile and o-cyanobenzamide.

Applications

MPC complexes exhibit electrocatalytic activity towards redox reactions due to their ability to retain their molecular structure when adding or removing electrons. These compounds are excellent electrocatalysts and have established themselves as significant elements in applications such as thin film switches ^[110-111], gas sensors ^[112-113], solar cells, fuel cells, electrochromism, photochromism, optical memory ^[114], data storage devices ^[115], liquid crystal color displays ^[116], in photodynamic therapy of cancer ^[117] and field-effect transistors (FETs) ^[118]. Extensive work has been performed by Ozoemena and Nyokong regarding these compounds and the manipulation of the MPC for various applications ^[119].

Originally MPC complexes were primarily used as dyes and pigments however recent research has extensively focussed on their collaborative properties. Bulk phthalocyanine and other nanoparticles are hybridized together to form structures known as "nanohybrids" or "composites". These structures have been very popular



due to their enhanced sensitivity in electrocatalytic applications such as the detection of dopamine, epinephrine, pollutants and glucose ^[120]. However work relating to the electrocatalytic ability of nanostructured MPC complexes has not been extensively preformed ^[121].

1.5 MICROSCOPIC TECHNIQUES

1.5.1 ELECTRON MICROSCOPY

This form of microscopy uses an electron beam to create an image of an analyte in which the magnification is greater than that of a light microscope. This amplification of light produces a technique with much higher resolution which allows much greater detail to be seen for smaller samples. The resolution increases due to the high speeds of the electrons and from this stems two types of electron microscopes, the transmission electron microscope (TEM) and scanning electron microscope (SEM). TEM involves shooting a high voltage beam through a thin layer of sample and obtaining information about the structure. SEM in contrast produces images by detecting secondary electrons or backscattering electrons that have been emitted off the surface due to excitation by the primary electron beam. The secondary electrons have a lower energy and can be used to describe the texture and roughness of the surface. In SEM, the electron beam across the surface is scanned in a zig-zag pattern by mapping the detection signals with the beam positions. The disadvantage with these microscopic techniques is that they are very expensive to buy and maintain and they are sensitive to magnetic fields and therefore require a cool water supply constantly running through the lens alternatively liquid nitrogen can be used for cooling.



1.5.2 ATOMIC FORCE MICROSCOPY

The Atomic Force Microscope (AFM) was developed to produce three dimensional images of any surface type with a nanometre and Angstrom resolution, samples surfaces such as polymers, ceramics, composites, glass, and biological material. A laser beam deflection system is used in which a laser is reflected from the back of the reflective AFM cantilever and onto a position-sensitive detector. The AFM tips and cantilevers used are made of Si or Si₃N₄. The force is calculated by measuring the deflection of the lever of the surface of the sample however the stiffness of the cantilever must be considered.

1.5.3 ULTRAVIOLET SPECTROSCOPY

In a standard UV Visible spectrophotometer, a beam of light is split into 2 components, a reference beam and a sample beam. The reference beam is directed through a cell that just contains the solvent whereas the sample beam is shone through a sample containing the solvent and analyte. Different molecules absorb light at different wavelengths and the wavelength at which a sample will absorb UV or visible light depends on how easily an electron is promoted to a higher energy level, molecules that require more energy for electron promotion absorb at shorter wavelengths and those that require less energy do so at longer wavelengths.



CHAPTER 2

EXPERIMENTAL



2.1 MATERIALS AND REAGENTS

Mercaptopropionic acid (MPA) and Epinephrine (EP) were purchased from Fluka and Sigma, respectively. *N,N*-dimethylformamide (DMF) was obtained from Sigma-Aldrich, and was distilled and dried before use. Hexadecyl-trimethylammonium bromide (CTAB) was purchased from Sigma and used as a stabilizing agent. Ultra pure water of resistivity 18.2 M Ω .cm was obtained from a Milli-Q Water System (Millipore Corp., Bedford, MA, USA) and was used throughout for the preparation of solutions. Phosphate buffer solutions (PBS) at various pH were prepared with appropriate amounts of K₂HPO₄ and KH₂PO₄, and the pH adjusted with 0.1 M H₃PO₄ or NaOH. All electrochemical experiments were performed with argon-saturated 0.1 M PBS (pH 7.4). All other reagents were of analytical grades and were used as received from the suppliers without further purification. Experiments were performed at 25 \pm 1 $^{\circ}$ C.

Multi-walled carbon nanotubes (MWCNT) were obtained from Sigma. The MWCNT were first purified and cut into short and uncapped nanotubes, bearing sulphonic functional groups (psf-MWCNT) according to the multi-step procedure developed by Smalley and co-workers ^[122] (scheme 1:step 2). The procedure was as follows; 2 M HNO₃ solution was prepared by mixing 24.84 ml of HNO₃ (15.69 M) in 125 ml Deionised (DI) water in a 200 ml round bottom flask. 650 mg MWCNT was refluxed in the 2.6 M HNO₃ for 17 hrs at 90 $^{\circ}$ C.

The purified MWCNT (p-MWCNT) were then cleaned by centrifugation at 7500 rpm for 30 mins. The acid was decanted and disposed in acid waste bottles. Using a vortex, the particles were washed with DI water and vacuum filtrated in a Buchner



filtration system. The p-MWCNT were dried, weighed and stored at room temperature. The p-MWCNT was further functionalised by sonication. 60 ml H₂SO₄ and 20 ml HNO₃ were added in a 100 ml beaker to produce the acid solution. The reaction was exothermic and the beaker heated up significantly therefore an ice bucket was used to cool the acid solution. Care was taken not to allow any water to enter the acid solution. 30 mg of p-MWCNT was suspended in the 80 ml H₂SO₄:HNO₃ (3:1 v/v) acid solution and the suspension was placed in the sonicator for 14 hrs at 40-50°C .

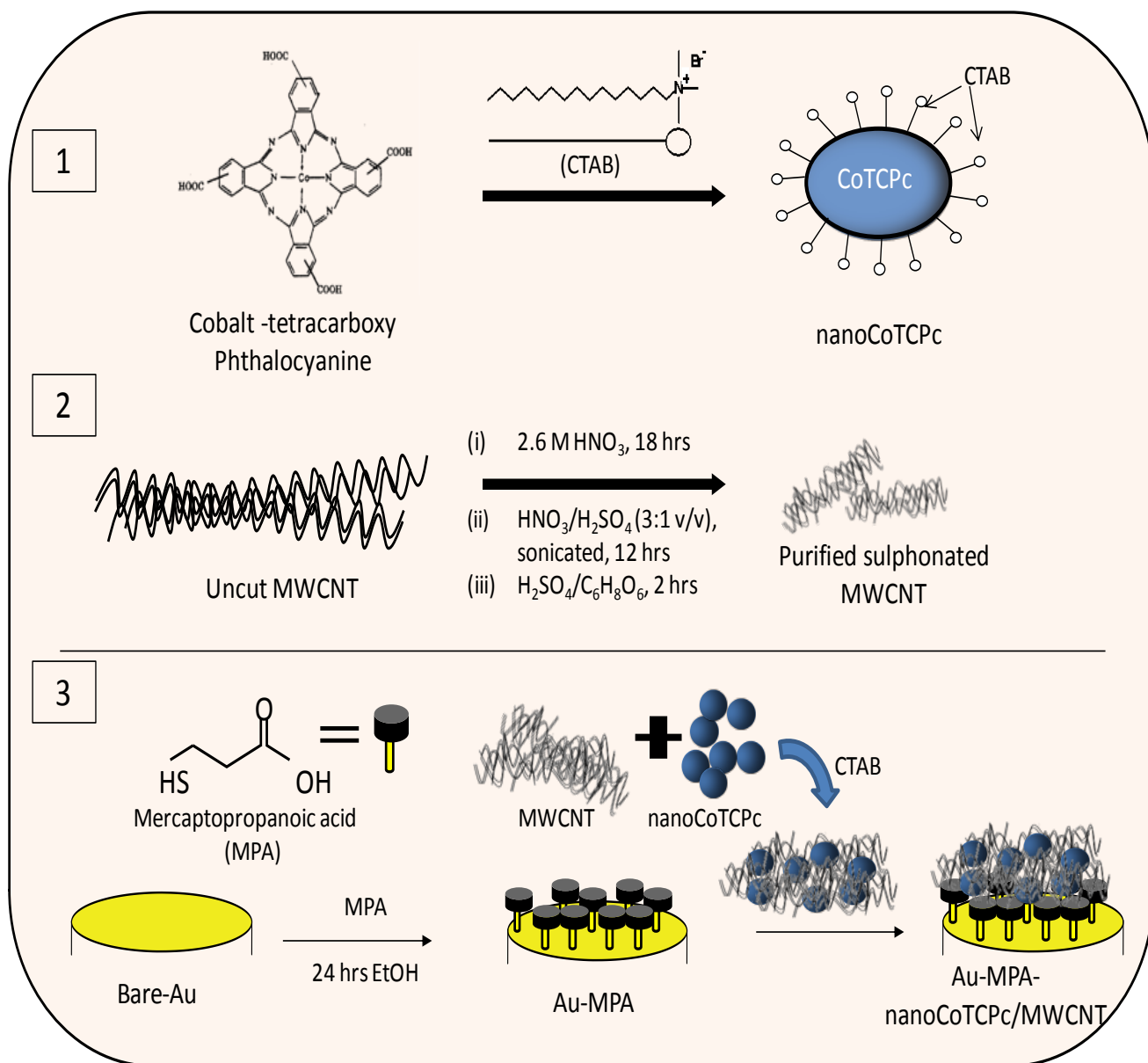
A 10 mg: 25 ml ratio of p- MWCNT was used to cater for a slightly wet sample as well as preparation of a larger final mass product. The suspension was left undisturbed overnight in which the purified and functionalised MWCNT (pf-MWCNT) settled at the beaker base. The liquid was decanted and disposed in an acid waste bottle. The pf-MWCNT were centrifuged at 7500 rpm for 20 mins to remove the remaining acid followed by further washing with DI water using a vortex. A TPP filter map was used to filter the pf-MWCNT suspended in DI water, until the outlet water was neutral on pH paper. The pf- MWCNT were vacuumed dried for 18 hrs. The product was weighed and stored at room temperature. The addition of sulphur groups has been proven to be an ideal method of functionalisation of MWCNT as it forms covalent and non-covalent bonds thus enhancing the response during detection ^[123]. Therefore 20 ml of Sulphuric acid (98.08 g/mol, H₂SO₄) was added slowly to 300 ml Acetic Anhydride (102.09 g/mol, C₄H₆O₃) in a 500 ml beaker. 100 mg of pf-MWCNT was weighed and added to the solution. The suspension was placed on a heating mantle and stirred for 2 hrs at 70°C. The solution was then cooled to room temperature whilst continuing to stir.



The sulfonated pf-MWCNT (pfs-MWCNT) were then washed with distilled water by 4 centrifuge cycles and the final product dried in a vacuum oven at 40⁰C. The pfs-MWCNT used in all hybrid synthesis will here from be referred to as MWCNT.

The synthesis of the initial hybrid (**AuNP/MWCNT**) was preformed according to Zhang et al ^[124]. A trisodium citrate solution was prepared with 500 mg trisodium citrate (258.06 g/mol, Na₃C₆H₅O₇) in 50 ml DI water. A 0.57% HAuCl₄ solution was prepared by adding 57 mg HAuCl₄ (200.31 g/mol) in 10 ml DI water in a 10 ml volumetric flask. 3 mg MWCNT was added to 4 ml sodium citrate solution in a 250 ml Erlenmeyer flask and sonicated for 15 mins until the solution was homogenised. 96 ml DI water was then added to the solution. The mixture was stirred and heated to 100⁰C. Upon boiling, 0.5 ml of the 0.57 % HAuCl₄ solution was injected into the solution. Thereafter the solution was stirred for 2 hrs and further cooled for 24 hrs before storage at room temperature.

The second nanohybrid consisted of MWCNT coated in AuNR (**AuNR/MWCNT**). The AuNR was prepared using the seed mediated growth methodology, however the specific concentrations are Mintek confidential and therefore this seed mediated growth methodology will not be elaborated on. 1 ml of AuNR was mixed with 1 mg/ml MWCNT and sonicated for 6 hrs.



Scheme 1. 1 A Schematic illustration of the preparation and modification of the Au-nCoTCpC/MWCNT electrode. (1) Synthesis of nCoTCpC, (2) Synthesis of the functionalized MWCNT and (3) hybrid synthesis and electrode modification



The final solution was there stored at room temperature. In preparation of a newly designed hybrid (**nCoTCPc/MWCNT**), 1 mg nCoTCPc and 1 mg MWCNT was weighed and dissolved in 3 ml concentrated H₂SO₄ (98%). 0.45 g CTAB was dissolved in 300 ml DI water (CTAB solution). The nCoTCPc: MWCNT: H₂SO₄ solution was added drop wise into the CTAB solution in an ultrasonic ice-water bath. The solution was sonicated throughout the mixing process and produced a greenish black solution. This technique is commonly referred to as a one pot synthesis strategy. This technique improves the efficiency of a chemical reaction as it involves the simultaneous addition of all reactants together. The solution was ultra-centrifuged to separate the product and acidic solution. The tubes were decanted and the resulting suspension washed with DI water until neutral. The final product was dried in nitrogen then weighed and stored at room temperature. The final product was nanosized CoTCPc, and is referred to as nCoTCPc.

2.2 ELECTRODE MODIFICATION AND PRE-TREATMENT.

The gold electrode was pre-treated prior to each electrochemical experiment. Initially a solution of KOH was prepared by adding 2.80 g of KOH to 100 ml of DI water. The electrode was connected to a potentiostat and run in the 0.5 M KOH solution in order to desorb the impurities on the electrode surface. Desorption is an occurrence whereby a substance is released from or through a surface. The potential sweep moves in the opposite direction therefore from reduction to oxidation thus more negative to positive potential values. The electrodes are then polished on 0.3 μM alumina silica mats, followed by a 2 mins sonication in absolute ethanol. A pinraha solution was then prepared by combining 2 ml of peroxide and 6 ml of H₂SO₄ (3:1 ratio). This solution is used as peroxide is an excellent oxidizing



agent therefore the solution will oxidize the contaminants off the surface. The electrodes are dipped in the solution for 2 mins and washed thoroughly with DI water afterwards. Finally the electrodes are electrochemically cleaned in 0.5 M H_2SO_4 , (-0.5 V - 1.5 V).

AuNP/MWCNT , AuNR/MWCNT and nCoTCpC/MWCNT modified gold electrodes were prepared using SAMs. As the connection between the electrode and hybrid material is electrostatic, a thiol linker was required. The clean gold electrodes were immersed in a 4 mM MPA solution for 24 hrs thus forming a uniform and compact thiol monolayer. The MPA solution was prepared in ethanol, this effectively deprotonated the molecule resulting in a charged thiol monolayer on the electrode surface, onto which the modification material was electrostatically attached.

2.3 EXPERIMENTAL EQUIPMENT

All electrochemical experiments were carried out using an Autolab Potentiostat PGSTAT 302 (Eco Chemie, Utrecht, Netherlands) driven by the GPES (General Purpose Electrochemical System) and FRA (Frequency Response Analyser) software version 4.9. Electrochemical impedance spectroscopy (EIS) measurements were performed between 1.0Hz and 10 kHz using a 5 mV rms sinusoidal modulation in a solution of 1 mM of $\text{K}_4\text{Fe}(\text{CN})_6$ and 1 mM $\text{K}_3\text{Fe}(\text{CN})_6$ (1:1) mixture containing 0.1 M KCl, and at the $E_{1/2}$ of the $[\text{Fe}(\text{CN})_6]^{3-/4-}$ (0.124 V vs Ag|AgCl in saturated KCl). The FRA software allowed the fitting of the raw EIS data to equivalent circuit models using a complex non-linear least squares (CNLS) method.

Gold electrode (BAS, $r = 0.8$ mm) was used as the working electrode. Ag|AgCl in saturated KCl and platinum electrodes were used as pseudo-reference



and counter electrodes, respectively. A bench pH/ISE ORION meter was used for pH measurements. High resolution transmission electron microscopy (HRTEM) images were obtained from JEOL JEM 2100F (Japan). Conductivity and zeta potential (effective surface charge) was measured by dynamic light scattering using Zetasizer® Nano ZS equipment (Malvern PCS Instruments, UK). The samples were run in a DST1060C clear disposable zeta cell at room temperature with an equilibration time of 60 sec. Each sample was repeatedly measured 3 times and the values reported are the mean value \pm SD for two replicate samples.



CHAPTER 3

RESULTS AND DISCUSSION

3.1 PRE-TREATMENT OF GOLD ELECTRODES

The state of the gold electrode surface has been emphasised as a significant factor that influences the formation of high-quality reproducible self-assembled monolayers on a gold electrode [125]. Figure 3.1 illustrates the desorption voltammogram in 0.5 M KOH solution, in which 10 cycles were performed. The decrease in current response (shown by the direction of the arrow in Figure 3.1) shows the desorption of impurities on the electrode surface. All electrodes were cleaned in 1.0 M H₂SO₄ before further modification. Figure 3.2 shows the ideal cyclic voltammogram for a clean gold electrode surface.

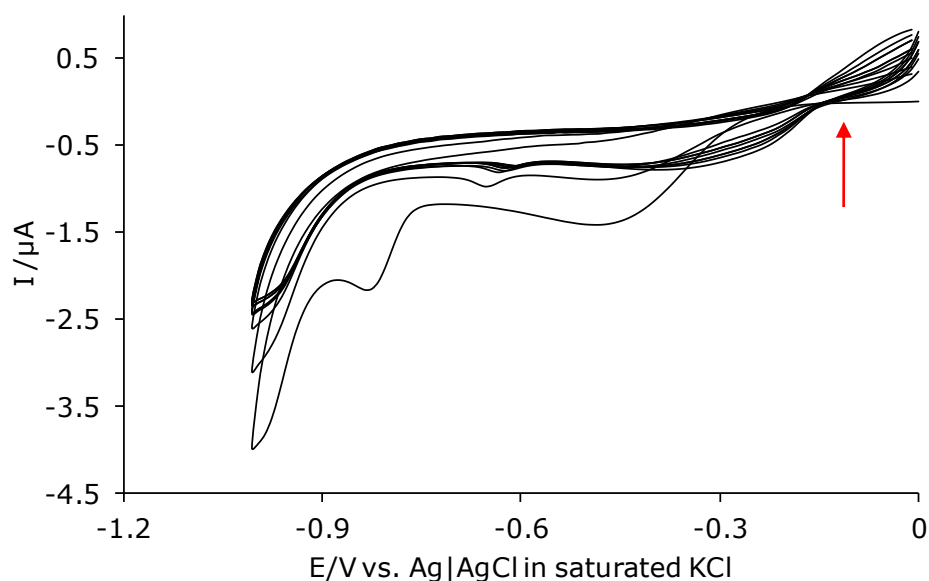


Figure 3. 1 Cyclic voltammogram in 0.5 M KOH illustrating the desorption profile of impurities off the gold electrode surface at 25 mV.s⁻¹

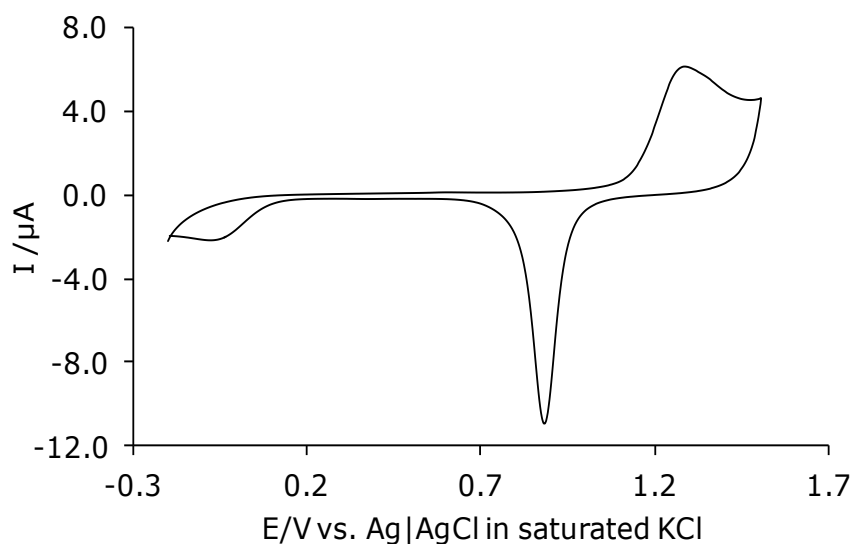


Figure 3. 2 A typical Cyclic voltammogram of a freshly cleaned gold electrode surface at $25 \text{ mV}\cdot\text{s}^{-1}$ in $0.5 \text{ M H}_2\text{SO}_4$

3.2 ANALYSIS OF HYBRIDS

The following section discusses characterisation and electrochemical methodologies used to investigate the 3 synthesised hybrids: AuNP/MWCNT, AuNR/MWCNT and nCoTCPc/MWCNT.

3.2.1 AuNP/MWCNT HYBRID

(a) CHARACTERISATION

TRANSMISSION ELECTRON MICROSCOPY

Figure 3.3 shows the TEM image of the assembly of AuNP onto the surface of MWCNT. An isolated example of the AuNP/MWCNT hybrid (Figure 3.3 (a)) is shown at approximate $\times 50\text{k}$ magnification. Figure 3.3 (a) shows that the AuNP are uniformly spread along the MWCNT and have a consistent diameter between 17-20 nm.

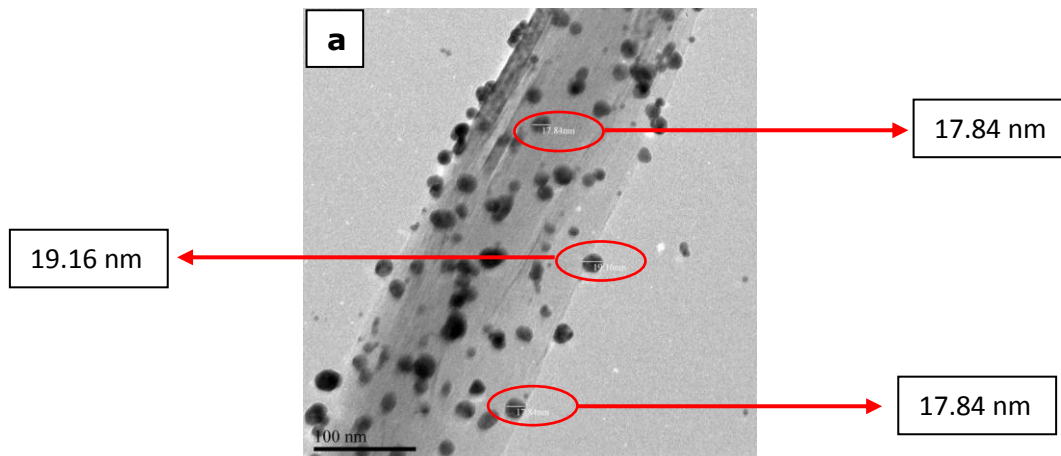


Figure 3.3 TEM illustrations of (a) the AuNP/MWCNT hybrid ($\sim x50k$ mag.)
(*mag.* = magnification)

ULTRAVIOLET VISIBLE SPECTROSCOPY

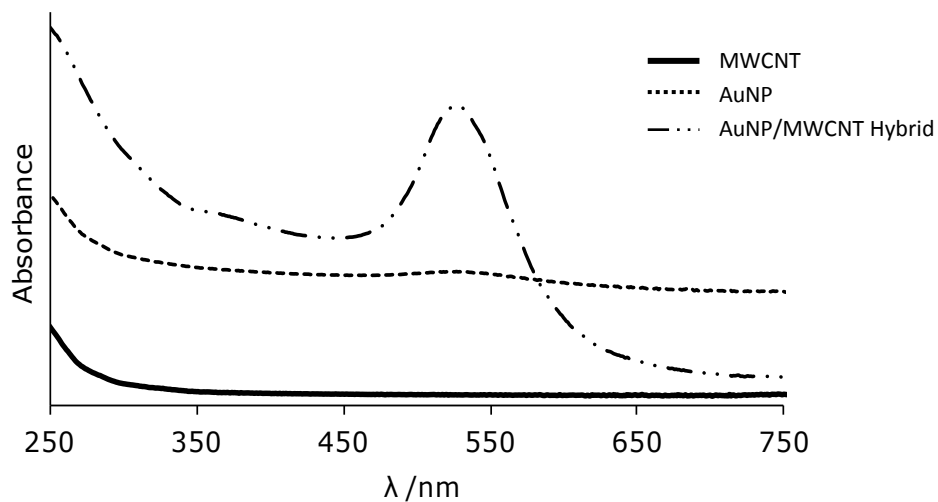


Figure 3.4 UV Visible spectrum for (i) MWCNT, (ii) AuNP and (iii) AuNP/MWCNT hybrid in pH 7.4 PBS solution

Figure 3.4 compares the UV visible spectra of (i) MWCNT, (ii) AuNP and (iii) AuNP/MWCNT in a pH 7.4 PBS solution (1 ml nanomaterial/ 3 ml pH 7.4 PBS). The



AuNP shows the strongest absorption peaks at a wavelength of 530 nm, as expected for AuNP ^[126]. The MWCNT showed no absorbance and the hybrid species shows a decreased absorbance relative to the AuNP. This can be attributed to the change in transparency of the AuNP/MWCNT hybrid in comparison to the AuNP and MWCNT components.

During my experiments, the AuNP/MWCNT hybrid continuously showed inconsistent results and for this reason no further investigations were carried out using this material.

3.2.2 AuNR/MWCNT HYBRID

(a) CHARACTERISATION

TRANSMISSION ELECTRON MICROSCOPY

Figure 3.5 shows the TEM image of the attachment of AuNR onto the surface of the MWCNT at an approximate x50k magnification. Sulphonated MWCNT in a pH 7.4 solution are deprotonated and thus have a net negative charge on their surface. This allows the cationic CTAB coated AuNR to electrostatically attach to the surface. From the TEM image, the average length of the AuNR was approximately 10 nm. The AuNR attached to the MWCNT via a side-to-side orientation, due to the orientation of the CTAB molecule.

The CTAB coverage of the AuNR is uniform and compact along the longitudinal sides however at the ends of the tubes, the CTAB is less compact and ordered leaving the AuNR more exposed ^[127]. This results in a consistent charge distribution along the longitudinal sides, hence electrostatic attraction between the longitudinal

sides is the preferential side of attachment. Since the AuNR is more exposed on the spherical ends, with the correct linker one can theoretically join the AuNR into a long chain based on intermolecular bonding ^[128] however this end to end linking was not seen during our synthesis of AuNR. From the TEM image in Figure 3.5, the AuNR attached to the MWCNT in a scattered and non-uniform manner.

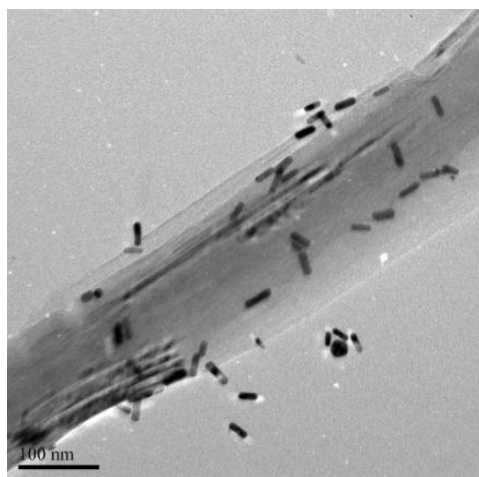


Figure 3. 5 TEM image of AuNR assembled on MWCNT (~x50k mag.)

(*mag.* = *magnification*)

ZETA POTENTIAL

Zeta potential is one of the main forces that mediate inter-particle interactions and it is measured by applying an electric field across the dispersion. The zeta potential values are analysed based on their absolute values. According to Table 3.1, the Zeta potential values for the AuNR (37 mV) and AuNR/MWCNT hybrid (22 mV) are relatively high. These values indicate that the small particles do not aggregate but rather remain suspended in solution. The zeta potential value of the MWCNT was



7.87 mV, a much lower value relative to AuNR and AuNR/MWCNT hybrid, which indicates that the material will settle out of solution. Visual observations of all the material supported the zeta potential values.

The solubility of the AuNR/MWCNT hybrid can be attributed to CTAB coating the AuNR. CTAB is a soluble surfactant that crystallises upon cooling, the CTAB coated AuNR hold the hybrid together. At temperatures lower than room temperature, the AuNR/MWCNT hybrid in solution will partially crystallise however it will remain in solution. The extent of crystallization is directly proportional to the dilution factor of the hybrid solution.

Table 3. 1 The zeta potential and conductivity values obtained for (a) MWCNT, (b) AuNR and (c) AuNR/MWCNT

	Materials	Zeta potential (mV)	Conductivity (mS/cm)
a	MWCNT	7.87	0.53
b	AuNR	37	0.03
c	AuNR/MWCNT	22	2.28

The conductivity value obtained can be used to compare the bulk AuNP and MWCNT material to the AuNP/MWCNT hybrid. It is evident from these values that the AuNR/MWCNT hybrid ($2.28 \text{ mS}\cdot\text{cm}^{-1}$) shows an enhanced conductivity relative to the AuNR ($0.03 \text{ mS}\cdot\text{cm}^{-1}$) and the MWCNT ($0.53 \text{ mS}\cdot\text{cm}^{-1}$). This indicates that upon formation of the AuNR/MWCNT hybrid, new properties and characteristics are present. The increased conductivity of the hybrid confirms that the integration of these two conductive materials form a remarkably conductive hybrid.



ELECTROCHEMICAL IMPEDANCE SPECTROSCOPY

Figure 3.6 (b) represents typical Nyquist plots obtained at the formal potential of the electrodes as seen from the CVs (Figure 3.6 (a)). Nyquist plots ($Z_{\text{imaginary}}$ vs. Z_{real}) are shown in Figure 3.6 for the AuNR, MWCNT and the AuNR/MWCNT hybrid in 0.1 KCl containing equimolar mixture of $K_4Fe(CN)_6$ and $K_3Fe(CN)_6$. Nyquist plots of the modified electrodes (Figure 3.6) showed a semicircle at the high frequency region and a straight line at the low frequency region. The semi circle indicates the redox reaction is kinetically controlled and is an indicator of the charge transfer resistance. The charge transfer resistance trend was observed as follows; Bare-Au < Au-MPA-AuNR < Au-MPA-MWCNT < Au-MPA-AuNR/MWCNT < Au-MPA.

At pH 7.4, the CTAB is deprotonated and has a positive surface polarity ^[1]. Therefore the Au-MPA-AuNR and Au-MPA-AuNR/MWCNT show an enhanced electron movement due to the attraction of the cationic surface and the anionic solution. However Figure 3.5 shows the AuNR are not uniformly spread along the MWCNT. This inconsistency was reflected in irregular EIS data. Therefore no further impedametric analysis was preformed on this material.

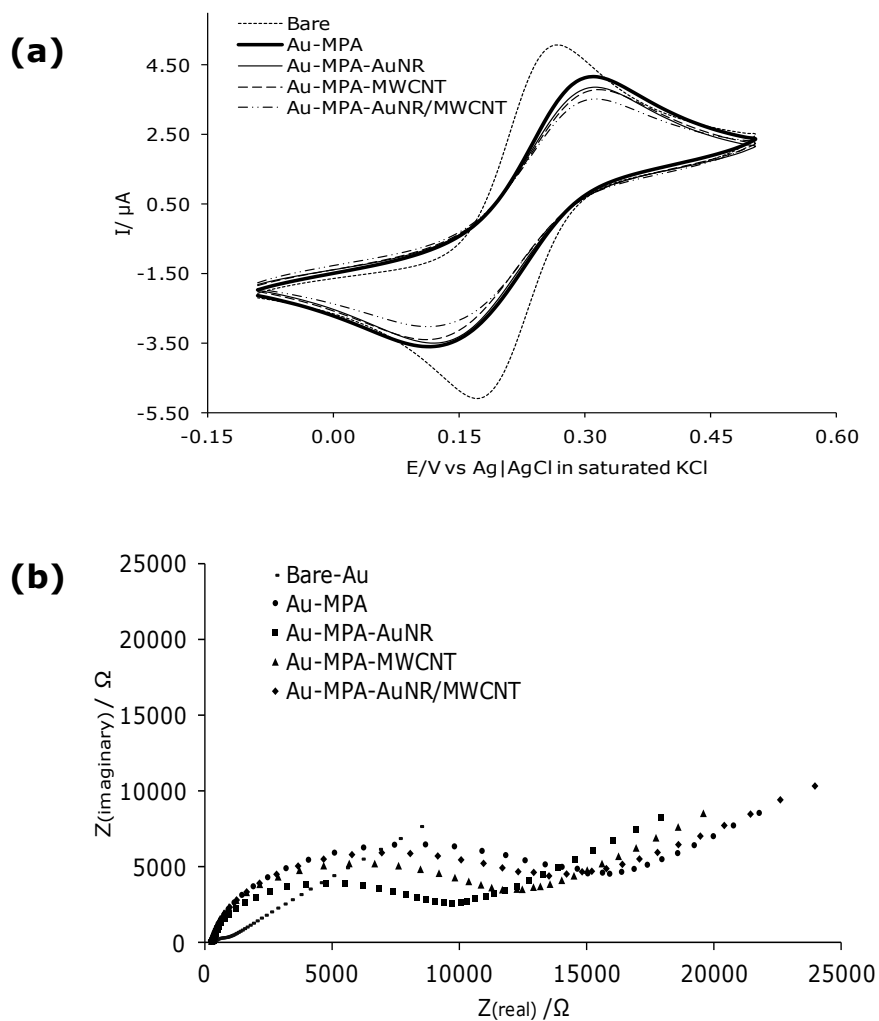


Figure 3.6 Comparative EIS parameter data obtained for Bare-Au, Au-MPA, Au-MPA-AuNR, Au-MPA-MWCNT and Au-MPA-AuNR/MWCNT in a (a) Cyclic voltammogram and (b) Nyquist plots in 0.1 KCl containing equimolar mixture of $\text{K}_4\text{Fe}(\text{CN})_6$ and $\text{K}_3\text{Fe}(\text{CN})_6$



(b) ELECTROCATALYTIC DETECTION

The electrocatalytic ability of the AuNR/MWCNT hybrid was investigated by comparing the electrocatalytic response in the absence (Figure 3.7 (a)) and presence (Figure 3.7 (b)) of 50 μM EP in pH 7.4 PBS. Figure 3.7 (a) compares the cyclic voltammograms of Bare-Au, Au-MPA-AuNR, Au-MPA-MWCNT and Au-MPA-AuNR/MWCNT. The current response shown by the AuNR/MWCNT hybrid is higher than the AuNR and MWCNT materials. Figure 3.7 (b) shows the electrochemical response in the presence of 50 μM EP in pH 7.4 PBS. The typical epinephrine redox processes were observed, with one irreversible peak at the anodic window and one reversible couple at the cathodic window.

According to Figure 3.7 (b), the current response was observed as follows; Au-MPA-AuNR/MWCNT (0.44 μA) > Au-MPA-MWCNT (0.42 μA) > Au-MPA-AuNR (0.39 μA) > Bare-Au (0.31 μA). The current response by the AuNR/MWCNT hybrid (0.44 μA) was greater when compared to the AuNR (0.39 μA) and MWCNT ((0.42 μA) materials, indicating the advanced properties of the AuNR/MWCNT hybrid. This trend in Figure 3.7 (b) was supported by Figure 3.7 (a), confirming the superior properties of the AuNR/MWCNT hybrid when compared to the AuNR and MWCNT.

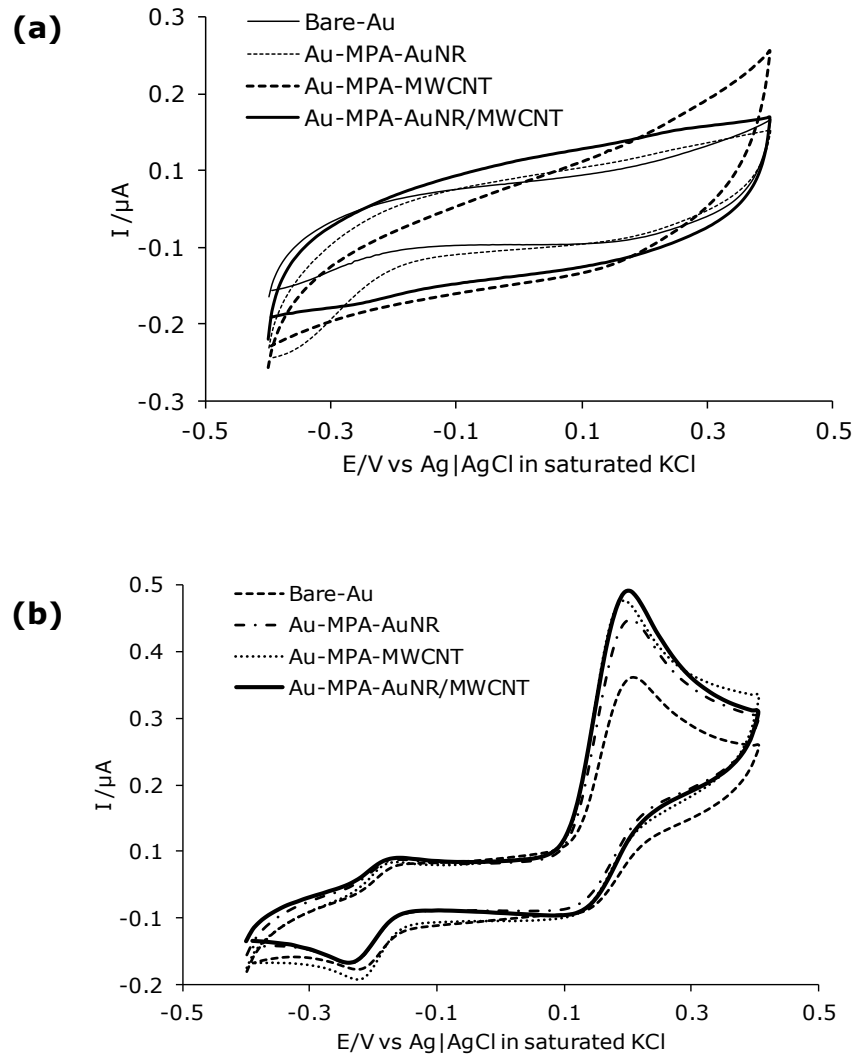


Figure 3.7 Cyclic voltammetric profiles of the different electrodes in the (a) absence and (b) presence of 50 μM EP in PBS pH 7.4 as a scan rate of 25 mVs^{-1}

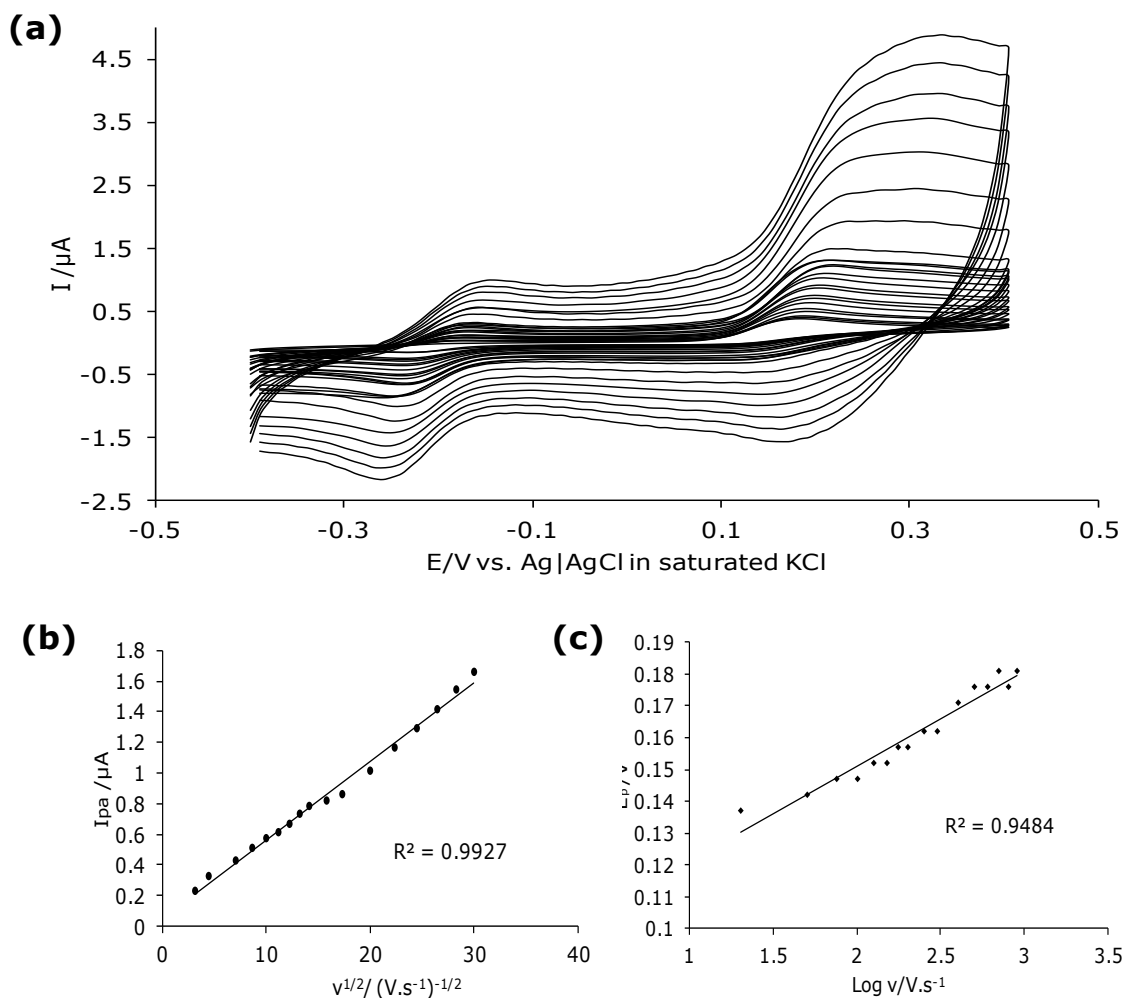


Figure 3.8 (a) Cyclic voltammograms of increasing scan rates (5 – 300 mV.s^{-1}) for 10 mM EP in PBS pH 7.4 for Au-MPA-AuNR/MWCNT (b) Plot of peak current (I_p) vs. square root of scan rate ($v^{1/2}$) and (c) plot of peak potential (E_p) vs. log of scan rate (v) from scan rate data

The scan rates were investigated to determine the electron transfer process at a constant concentration of 50 μM EP in pH 7.4 PBS. The CV evolutions (Figure 3.8 (a)) show a steady increase in the anodic peaks (I_p). Figures 3.8 (b) and (c) were extrapolated from this data, Figure 3.8 (b) shows the plots of the peak anodic



current vs. square root of scan rate, this showed a linear relationship ($R^2 = 0.996$) with approximately zero intercept, this is indicative of a diffusion-controlled process ^[129]. As seen with figure 3.8 (a), the oxidation peak potential shifts towards a more positive potential as the scan rate increases, confirming the kinetic limitation of the electrochemical reaction ^[130].

LIMIT OF DETECTION

The AuNR/MWCNT hybrid showed promising catalytic results and therefore a further investigation was performed using chronoamperometry to identify the limit of detection. Figure 3.9 shows the chronoamperogram using the AuNR/MWCNT hybrid that was obtained for a series of EP concentrations (0.47–4.12 μM), The limited of detection was calculated as 0.5 s/m, in which s is the standard deviation of the intercepts and sensitivity and m of the plot of the linear peak current vs. the concentration of EP (Figure 3.9 insert) which were calculated to be $s = 190 \text{ nM}$ and $m = 6.88 \times 10^{-3} \text{ A M}^{-1}$.

The catalytic rate constant and diffusion coefficient in EP were also investigated. At intermediate times (0.0–2.0 s) of the chronoamperometric measurements, the catalytic currents (I_{cat}) were dominated by the rate of the electrocatalysed oxidation of EP, thus the rate constants for the chemical reactions between the biological analyte and redox sites of surface immobilised hybrid were determined using the established equation ^[131]:



$$\frac{I_{cat}}{I_L} = \pi^2 (kC_0 t)^{\frac{1}{2}} \quad (\text{Equation 3.1})$$

where I_{cat} and I_L are the currents of Au-MPA-AuNR/MWCNT in the presence and absence of EP, respectively. C_0 is the bulk concentration of the analyte, k and t are the catalytic rate constant ($M^{-1} s^{-1}$) and time elapsed (s). From the slopes of the plots of I_{cat}/I_L vs. $t^{1/2}$, over the concentration range 1.36 – 4.41 μM , the value of k was found to be $6.71 \times 10^6 \text{ cm}^3 \text{ mol}^{-1} \text{ s}^{-1}$ ($6.71 \times 10^3 \text{ M}^{-1} \text{ s}^{-1}$) for EP. Also, from the chronoamperometric data, the diffusion coefficient, D , was determined using the Cottrell equation represented in Equation 3.2:

$$I = \frac{nFAD^{\frac{1}{2}}C_0}{\pi^{\frac{1}{2}}t^{\frac{1}{2}}} \quad (\text{Equation 3.2})$$

The diffusion coefficient for the AuNR/MWCNT hybrid was calculated to be $1.69 \times 10^{-6} \text{ cm}^2 \text{ s}^{-1}$.

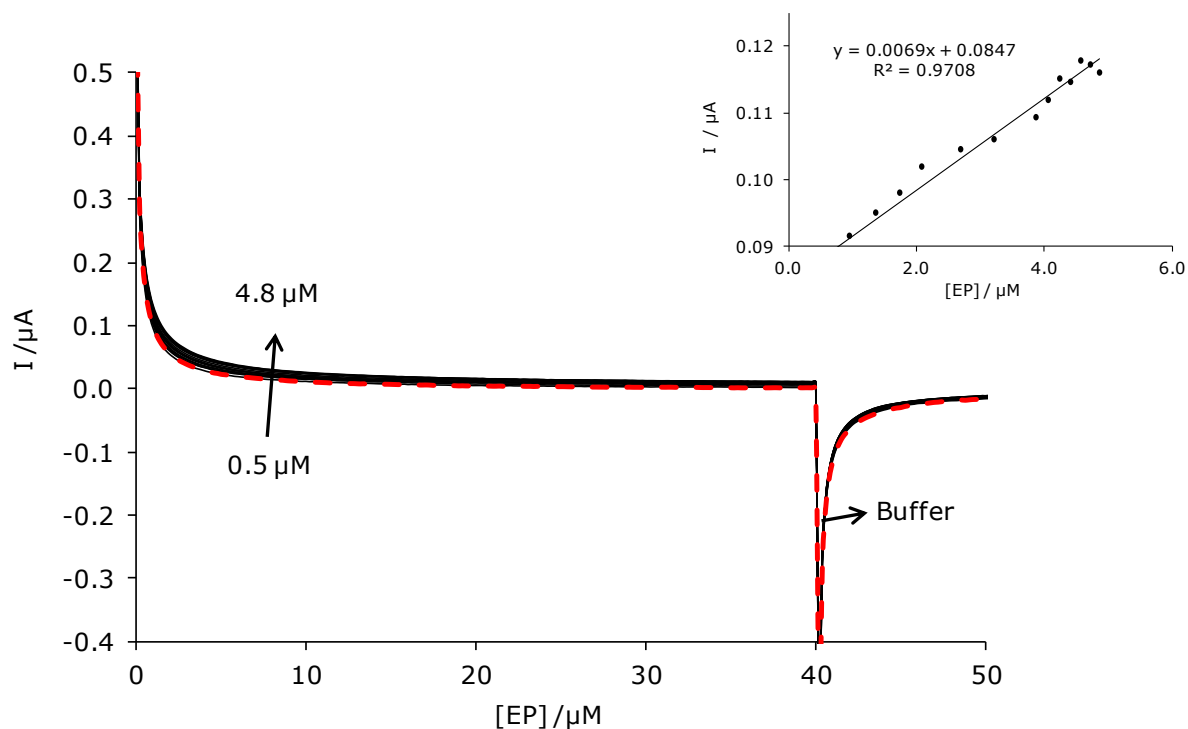


Figure 3. 9 Typical double potential step chronoamperometric transients at Au-MPA-AuNR/MWCNT in pH 7.4 PBS solution following addition of epinephrine. Concentration range (0.47–4.12 μM). Inset shows the plot of chronoamperometric current at $t = 1.2$ s vs. $[\text{EP}]$ at a scan rate of $25 \text{ mV}\cdot\text{s}^{-1}$

3.2.3 nCoTCPc/MWCNT HYBRID

(a) CHARACTERISATION

TRANSMISSION ELECTRON MICROSCOPY

Figure 3. 10 (a) and (b) exemplify comparative TEM images of CoTCPc and nCoTCPc, respectively. The size of the nCoTCPc was in 8 – 26 nm range while the CoTCPc particle was greater than 0.5 μm . From the size data, it is evident that the CoTCPc undergoes a reduction in size during the nanostructuring process, to form nCoTCPc. Figure 3. 10 (c) and (d) show TEM images of acid-treated MWCNT before

and after integration with nCoTCPc, respectively. The clear MWCNT (Figure 3. 10 (c)) can easily be distinguished from the stained MWCNT in the nCoTCPc/MWCNT hybrid material (Figure 3. 10 (e) and (f)). Figure (e) and (f) shows the entrapment of the nCoTCPc within the cylindrical structure as well as the attachment along the sidewalls of the MWCNT. This results from the electrostatic interactions between the individual species.

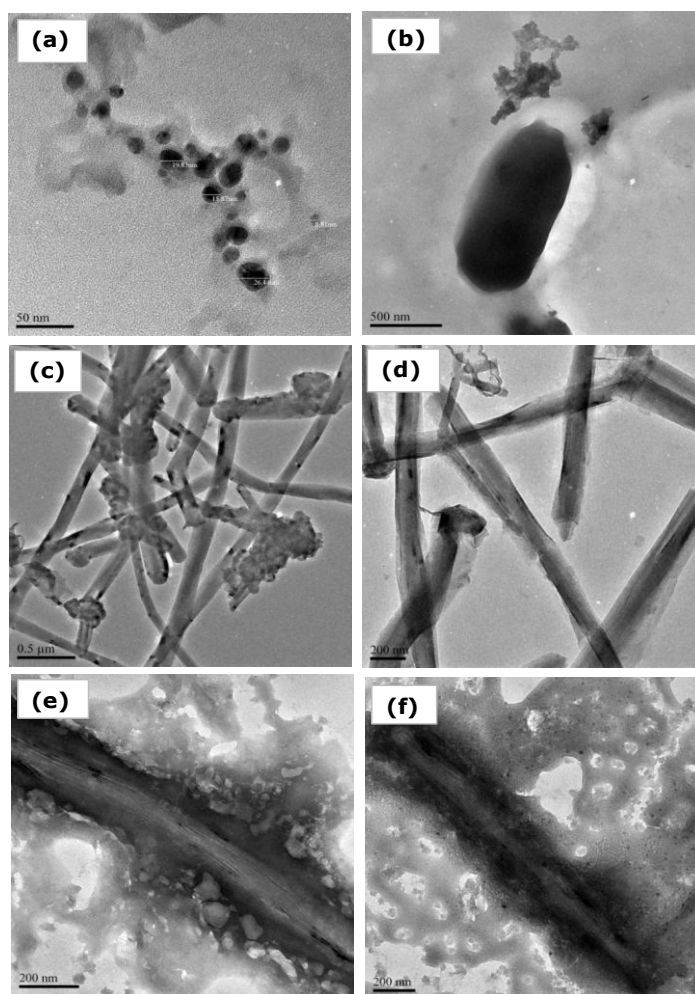


Figure 3. 10 TEM image of (a) CoTCPc (x6k mag.), (b) nCoTCPc (x50k mag.), (c)/(d) MWCNT (x10k mag.) and (e)/(f) nCoTCPc/MWCNT (x10k mag.)

(mag. = magnification)

ULTRAVIOLET VISIBLE SPECTROSCOPY

Figure 3. 11 compare the UV visible spectra of (i) nCoTCPc, (ii) MWCNT and (iii) nCoTCPc/MWCNT in a pH 7.4 PBS solution (1 ml nanomaterial/ 3 ml pH 7.4 PBS). The nCoTCPc has an oxidation state of +2 and shows the strongest absorption peaks at a wavelength of 680 nm. The strongest absorption peaks are assigned to the Q band, which could be attributed to the allowed π - π^* transition ^[132]. The B band is observed at a higher wavelength of 300 nm. The nCoTCPc/MWCNT hybrid complex shows a significant decrease in absorbance which may be attributed to the addition of MWCNT to the nCoTCPc. As expected, the MWCNT showed no absorbance peaks.

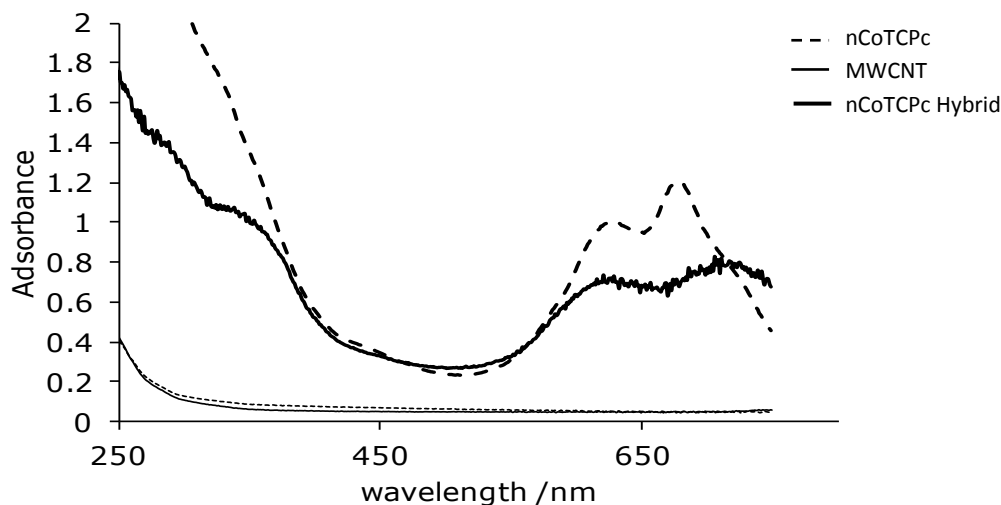


Figure 3.11 UV-visible spectra of (i) nCoTCPc, (ii) MWCNT and (iii) nCoTCPc/MWCNT



ATOMIC FORCE MICROSCOPY

AFM was employed to monitor the changes in surface morphology upon layer-by-layer assembly. The AFM images (Figure 3. 12 (a)-(h)) clearly depict an ultrathin film monolayer on the gold electrode; there is no significant difference between the thickness or the surface morphology of the bare and MPA-modified electrode. Also, upon modification with the individual materials or their composites, the surface roughness (SR) values were obtained from Figure 3.12 (b), (d), (f), (h) to be in the same magnitude: nCoTCPc/MWCNT (SR = 2.976 nm) > nCoTCPc (SR = 2.712 nm) > MWCNT(SR = 2.276 nm) > Bare-Au (SR = 2.145 nm). The vertical height for the nCoTCPc/MWCNT hybrid was *ca.* 10 nm.

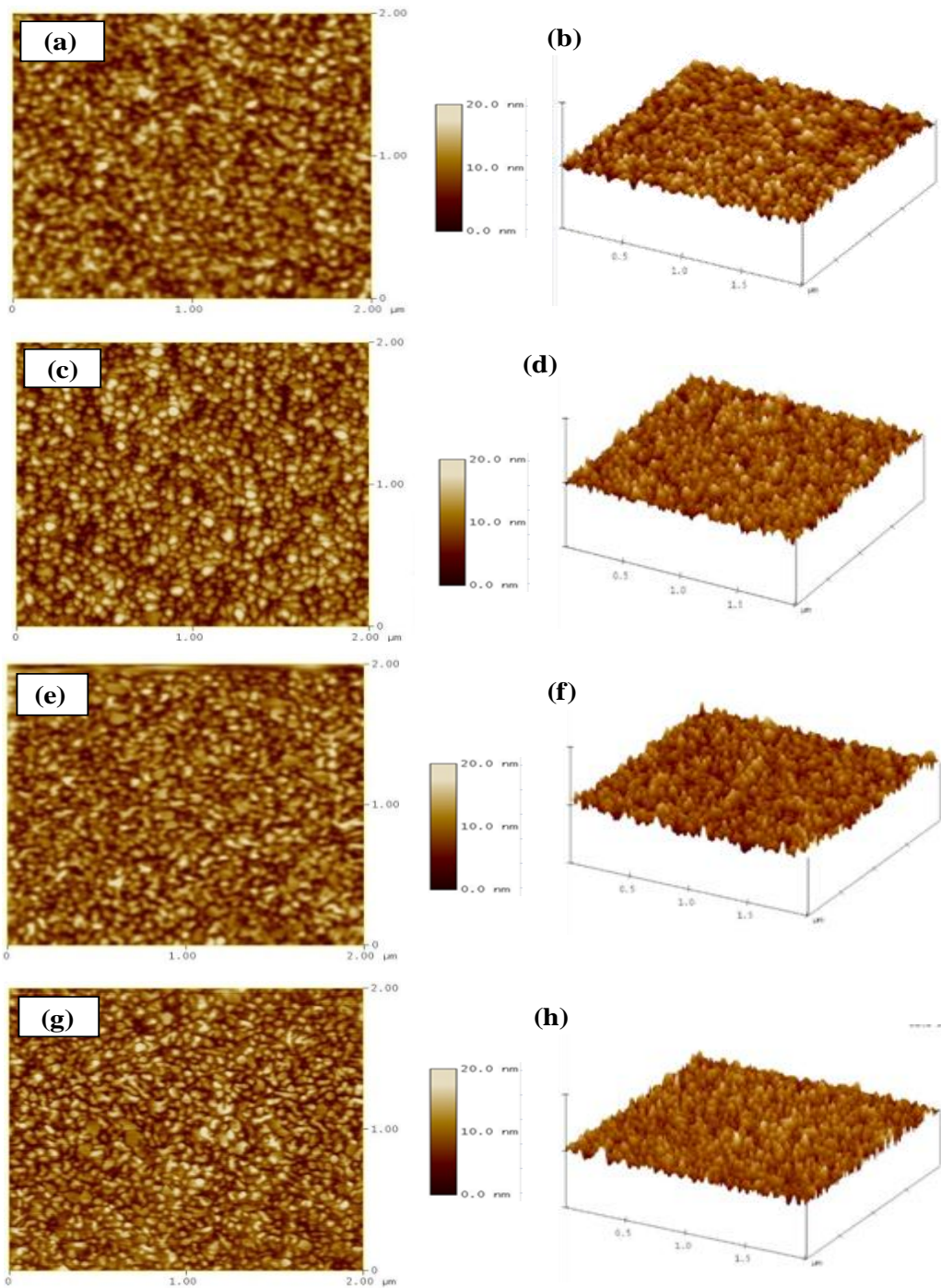


Figure 3. 12 AFM images of (a)/(b) Bare gold electrode, and gold-modified with (c)/(d) MWCNT, (e)/(f) nCoTCPc, and (g)/(h) nCoTCPc/MWCNT at room temperature



ZETA POTENTIAL

Table 3.2 shows the measured zeta potential of nCoTCPc, MWCNT and nCoTCPc/MWCNT. The zeta potential values of both nCoTCPc (5.37 mV) and MWCNT (7.87 mV) are less than 10 mV. This means the particles are not stable in solution (the same was confirmed visually when allowing the solutions to stand for 24 hrs). However, the nCoTCPc/MWCNT hybrid showed a high zeta potential of +31.7 mV (conventionally, a high zeta potential can be high in a positive or negative sense, i.e. <-30 mV and $>+30$ mV). This charge or magnitude of Zeta potential implies that there is going to be less interaction among the particles due to electrostatic repulsion hence less aggregation and particles remaining as discrete particles for a long period. Furthermore, the magnitude of zeta potential is not necessarily a function of size, but rather the surface chemistry of the material and hence indicative of the stability of particles in a suspension.

Table 3. 2 The zeta potential and conductivity values obtained for (a) MWCNT, (b) AuNR and (c) AuNR/MWCNT

	Materials	Zeta potential (mV)	Conductivity (mS/cm)
a	MWCNT	7.87	0.53
b	nCoTCPc	5.37	0.0043
c	nCoTCPc/MWCNT	31.70	15.0

It is possible that this excellent stability in aqueous environment results from (i) electrostatic interaction between the negatively-charged MWCNT and the positively-charged metallophthalocyanine, (ii) π - π interactions between these two remarkable π -electron species, and/or (iii) a network of intermolecular hydrogen



bond attraction between oxygen moieties on the MWCNT sidewalls and hydrogen molecules of alkane chain in the CTAB molecules that house the nCoTCPc. From the nano Zetasizer, we were also able to measure the conductivity of each material. The nanohybrid material demonstrated superior conductivity (15.0 mS cm^{-1}) in comparison to the nCoTCPc ($0.0043 \text{ mS cm}^{-1}$) and MWCNT (0.53 mS.cm^{-1}). The excellent results of the nCoTCPc/MWCNT composite from the nano Zetasizer (i.e., excellent charge stability in aqueous media and conductivity) suggest to us that this new nanocomposite material could exhibit faster heterogeneous electron transfer kinetics and charge-storage properties as in electrochemical capacitor. The next section describes our investigations on these two phenomena.

HETEROGENEOUS ELECTRON TRANSPORT (HET)

The HET was investigated using a popular redox probe, $[\text{Fe}(\text{CN})_6]^{3-}/[\text{Fe}(\text{CN})_6]^{4-}$ redox systems in 0.1 M KCl solution. Figure 3.13 compares the CV and EIS data of the various electrodes. Figure 3.13 (b) and (c) present typical Nyquist and Bode plots obtained at the formal potential of the electrodes as seen from the CVs (Figure 3.13 (a)). The EIS data were fitted using the Randles equivalent circuit of mixed kinetic and diffusion control (Figure 3.13 (b) inset). In the circuit, the constant phase element replaces double layer capacitance in describing the impedimetric data owing to the non-homogenous bare and modified gold surfaces, R_s represents the solution/electrolyte resistance, R_{ct} represents the charge-transfer resistance (domain of kinetic control) at the electrode/electrolyte interface, and Z_w is the Warburg impedance which is associated with the domain of mass transport resulting from the linear diffusion of redox probe ions from the bulk electrolyte.

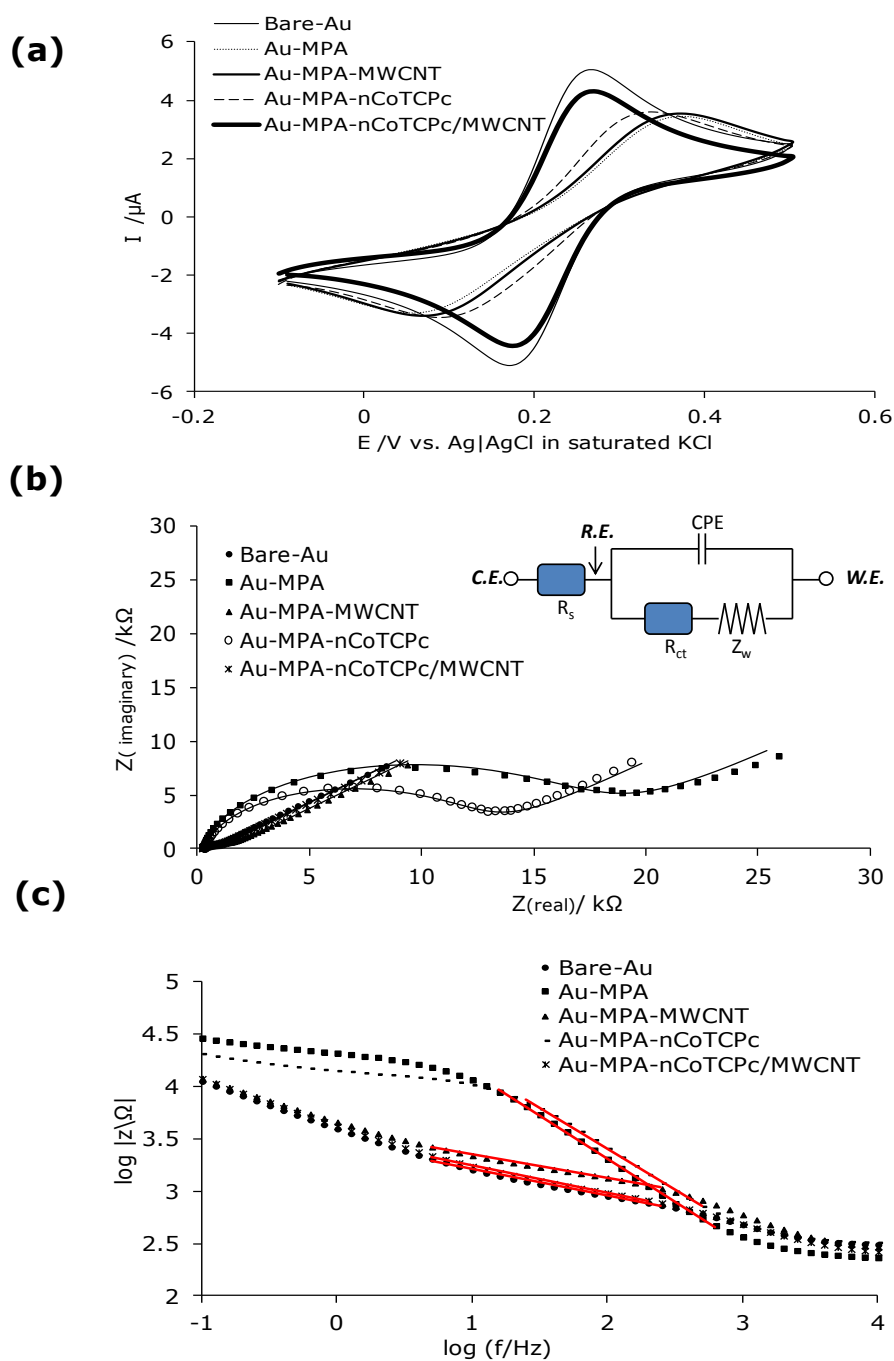


Figure 3. 13 Comparative EIS parameter data obtained for Bare gold, and gold-modified with MPA, MWCNT, nCoTCPc and nCoTCPc/MWCNT in a (a) Cyclic voltammogram, (b) Nyquist plots and (c) Bode plots in 0.1 KCl containing equimolar mixture of $\text{K}_4\text{Fe}(\text{CN})_6$ and $\text{K}_3\text{Fe}(\text{CN})_6$



From the data in Table 3. 3, R_{ct} values of the Bare Au and Au-modified with the nCoTCPc/MWCNT are approximately the same, indicating that truly a thin film of the nCoTCPc/MWCNT was formed on the gold electrode, corroborating our AFM data. Indeed, the impregnation of MWCNT with nCoTCPc plays an important role in accelerating the electron transfer process between $[\text{Fe}(\text{CN})_6]^{3-/4-}$ and the underlying gold surface. The high R_{ct} value of the base MPA-SAM is negatively charged with a surface pK_a of 5.2 ^[133]. Therefore, due to electrostatic repulsion, it is expected that the negatively charged Au-MPA at a pH of 7.4 would have the largest R_{ct} value. The Z_w values, which correspond to the diffusion process of the oxidised and reduced species of the $[\text{Fe}(\text{CN})_6]^{3-/4-}$ couple, are approximately of the same magnitude for all the electrodes. Ideally, R_s and Z_w should not be affected by modification of the electrode surface ^[134], the values obtained in this work are in the same magnitude, within limits of experimental errors. The higher CPE value indicates the nCoTCPc/MWCNT modified electrode provides a more uniform film in comparison to the other electrodes while the n values (< 1.0) indicate the electrodes are not true capacitors but rather pseudocapacitive in nature.

Table 3. 3 Summary of the electrochemical impedance spectroscopic evolutions \pm the standard deviation for the electrodes in $[\text{Fe}(\text{CN})_6]^{3-}/[\text{Fe}(\text{CN})_6]^{4-}$ redox systems in 0.1 M KCl solution

Au-electrode modifier	R_s / $\Omega\cdot\text{cm}^2$	CPE / $\text{mF}\cdot\text{cm}^{-2}$	n	R_{ct} / $\text{k}\Omega\cdot\text{cm}^2$	Z_w / $\mu\Omega\cdot\text{cm}^2$	$10^3 k_{app}$ ($\text{cm}\cdot\text{s}^{-1}$)
Bare-Au	5.49 \pm	193.05 \pm	0.85 \pm	0.009 \pm	2.28 \pm	26.53 \pm
	3.33	9.11	0.51	3.12	0.55	0.83
MPA	4.68 \pm	72.60 \pm 2.92	0.90 \pm	0.341 \pm	2.06 \pm	0.78 \pm
	1.24		0.47	1.39	4.05	0.01
nCoTCPc	6.39 \pm	54.04 \pm 2.79	0.90 \pm	0.241 \pm	2.32 \pm	1.09 \pm
	0.97		0.44	1.02	2.57	0.01
MWCNT	5.04 \pm	76.93 \pm 6.06	0.81 \pm	0.023 \pm	2.18 \pm	11.63 \pm
	1.06		0.88	1.29	0.44	0.15
nCoTCPc/ MWCNT	4.42 \pm	124.35 \pm	0.78 \pm	0.013 \pm	2.16 \pm	19.73 \pm
	1.56	8.65	1.72	2.72	0.45	0.54

The impedance (Z_{CPE}) is defined as ^[135]:

$$Z_{CPE} = \frac{1}{[Q(j\omega)^n]} \quad (\text{Equation 3.3})$$

where Q is the frequency independent constant relating to the surface electroactive properties, Ω is the radial frequency, n arises from the slope of $\log |Z|$ vs. $\log f$ (Figure 3.13 (c)) and has values: $-1 \leq n \leq 1$. An n value of zero corresponds to a pure resistor; a unit value of n corresponds to a pure capacitor; while a 0.5 value corresponds to Warburg impedance, associated with the domain of mass transport control arising from the diffusion of ions to and from the electrode|solution interface. The n values of the $\log |Z|$ vs. $\log f$ plots are in the 0.78 – 0.90 range meaning that these electrodes are pseudocapacitive in nature. In



addition, the phase angles were less than 90° , further confirming the pseudocapacitive nature of the electrodes.

CHARGE STORAGE PROPERTIES (ELECTROCHEMICAL CAPACITORS) IN AQUEOUS ENVIRONMENT

Figure 3. 14 compares the cyclic voltammetric responses of the bare Au electrode, nCoTCPc and nCoTCPc/ MWCNT modified electrodes in a buffer solution (PBS pH 7.4, shown as Figure 3.18 (b)) and acid solution (1M H₂SO₄, Figure 3. 14 (a)). In both aqueous systems, the nCoTCPc/MWCNT modified electrode gave the broadest voltammograms (i.e., capacitive currents). The voltammograms lack the rectangular features expected of an ideal electric double layer, but rather showed weak peaks in the region of +0.30 V (pH 7.4 buffer solution) and around 0.45 and 0.25 V (acid solution) due to the Co^{II}/Co^{III} redox processes.

Also note that the MWCNT modified electrode also shows a weak response in the +0.16 V region. Compton's group has observed similar peak and ascribed it to the surface oxo-groups (quinonyl oxygen functionalities) introduced during the functionalisation process of the MWCNT [136-137]. The results here clearly suggest that the nCoTCPc/MWCNT could be a viable material for pseudocapacitor operable in aqueous electrolyte.

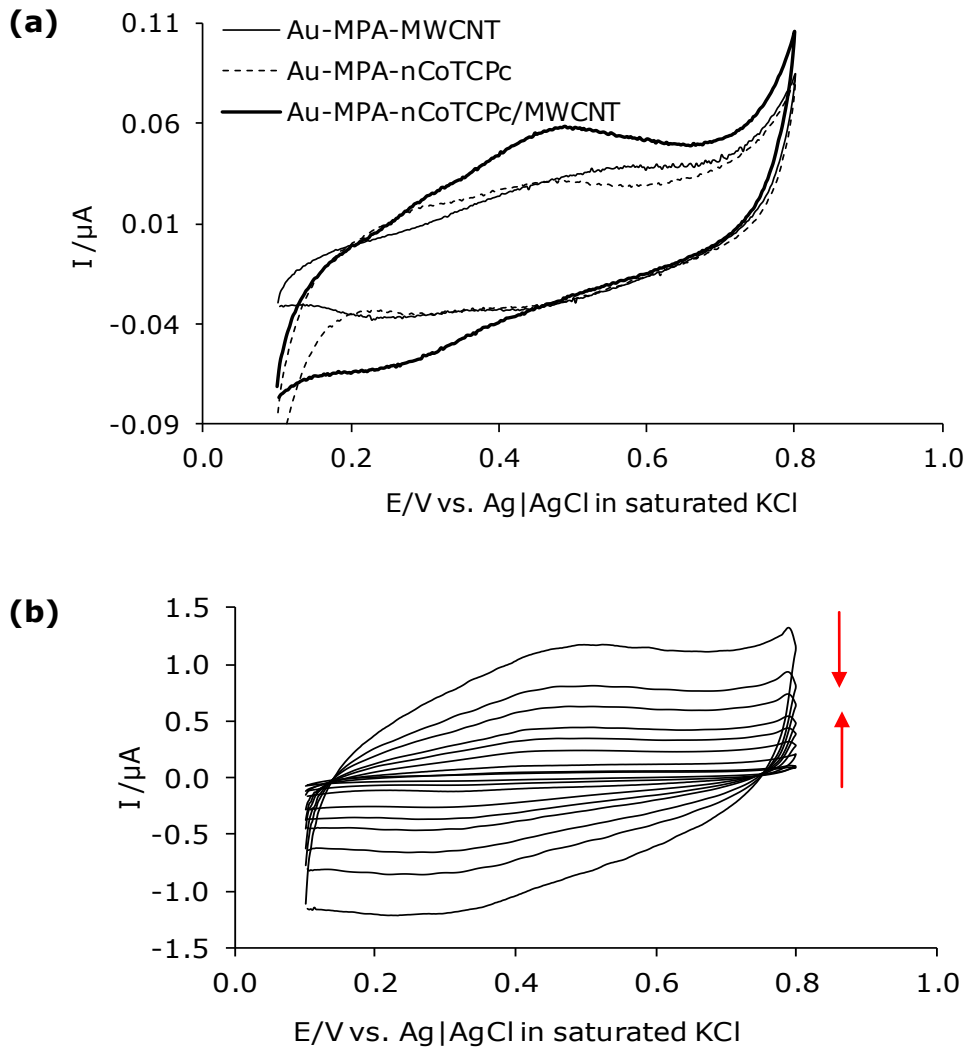


Figure 3. 14 Comparative cyclic voltammograms of the Bare Au electrode, nCoTCpC and nCoTCpC/MWCNT modified electrodes in (a) acidic solution (1M H₂SO₄). Figure (b) depicts the scan rate studies in acidic solution.

The voltammograms in the acid media show wider potential window (0.1 – 0.8 V) compared to the pH 7.4 solution (-0.1 – +0.5 V), meaning that the former should provide more energy density than the latter. Scan rate studies of the nCoTCpC/MWCNT in acid solution (Figure 3.14 (b)) gave well-defined increment in capacitive currents as the scan rate was increased ($\geq 300 \text{ mVs}^{-1}$), meaning that the

electrode, if used to fabricate a pseudocapacitor device, can allow the withdrawal of high current (i.e., excellent rate capability or power density). The capacitive behaviour is examined in detail using the more reliable galvanostatic charge/discharge strategy. The symmetrical curves of the graphs indicate that the materials (modifiers) show good capacitive behaviour.

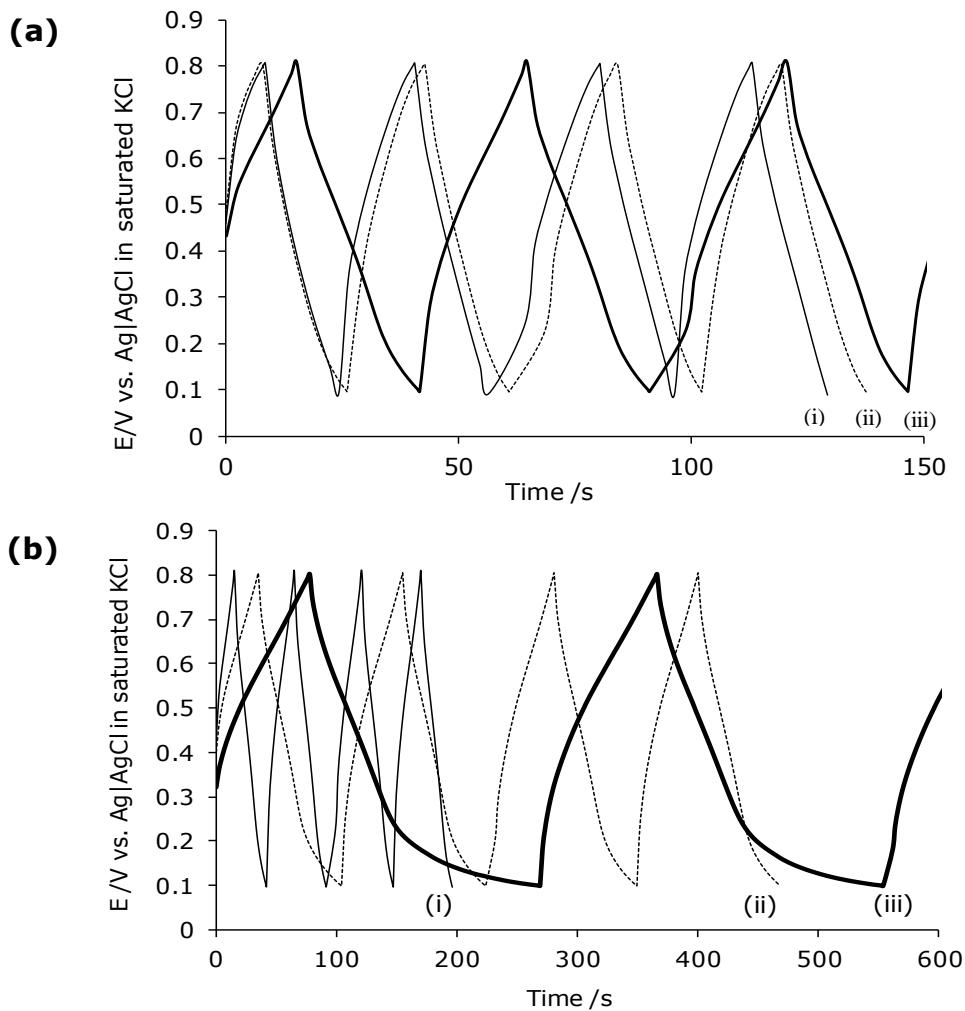


Figure 3.15 (a) Galvanostatic charge/discharge curves obtained for (i) nCoTCPc, (ii) MWCNT, and (iii) nCoTCPc/MWCNT. Figure 3.15 (b) illustrates the SC of nCoTCPc/MWCNT at current densities of 10, 5 and 3 $\mu A.cm^{-2}$



The specific capacitance (SC), specific energy density (E_{sp}) and specific power density (P_{sp}) are obtained using the conventional equations:

$$SC \text{ (F.cm}^{-2}\text{)} = \frac{I\Delta t}{A\Delta E} \quad \text{(Equation 3.4)}$$

$$P_{sp} \text{ (W.cm}^{-2}\text{)} = \frac{I\Delta E}{A} \quad \text{(Equation 3.5)}$$

$$E_{sp} \text{ (W.h.cm}^{-2}\text{)} = \frac{It\Delta E}{A} \quad \text{(Equation 3.6)}$$

where I is the discharging current, Δt is the discharging time (s), A is the geometric area of the electrode (cm^2) and ΔE is the discharge voltage difference. Table 3. 4 summarizes the pseudocapacitive data.

At a current density of $10 \mu\text{A.cm}^{-2}$, the capacitance trend follows as: nCoTCPc/MWCNT ($3.71 \times 10^{-4} \text{ F.cm}^{-2}$) > nCoTCPc ($2.57 \times 10^{-4} \text{ F.cm}^{-2}$) > MWCNT($2.28 \times 10^{-4} \text{ F.cm}^{-2}$). The power and energy densities follow similar trend. The variation in specific capacitance values of different samples is due to the differences in their microstructural properties. The MWCNTmodifier shows a slightly lower specific capacitance in comparison to the nCoTCPc. The enhanced specific capacitance of the nCoTCPc/MWCNT may be attributed to (i) the synergism between the nCoTCPc and MWCNT, (ii) electrode features (increased conductivity or porosity formed during the self-assembly strategy) that permit free movement of the solution ions to and from the electrode/solution interface and/or (iii) high surface area support provided by MWCNT for nCoTCPc.



Table 3. 4 Comparative data showing the specific capacitance, specific energy density and specific power density for the electrodes

Au-electrode modifier	SC/ F.cm⁻²	P_{sp}/ W.cm⁻²	E_{sp}/W.h.cm⁻²	Ref
MWCNT	2.28 x 10 ⁻⁴	3.43x10 ⁻³	6.27 x10 ⁻²	This work
nCoTCPc	2.57 x 10 ⁻⁴	3.55x10 ⁻³	5.77 x10 ⁻²	This work
nCoTCPc/MWCNT	3.71 x 10 ⁻⁴	3.54x10 ⁻³	9.37x10 ⁻²	This work
CNT based EDLC	50 x 10 ⁻⁶	-	3.6 x 10 ⁻¹	[138]
CNT “forest” film	7 x 10 ⁻³	-	-	[139]

Figure 3.15 (a) shows the charge/discharge of nCoTCPc/MWCNT at different charge densities viz. 10, 5 and 3 $\mu\text{A.cm}^{-2}$ in 1.0 M M H_2SO_4 . Unfortunately, the nCoTCPc and MWCNT did not show reproducible results at current densities of 5 or 3 $\mu\text{A.cm}^{-2}$. From Figure 3.15 (b), the SC of nCoTCPc/MWCNT at current densities of 10, 5 and 3 $\mu\text{A.cm}^{-2}$ is 0.371, 0.984 and 2.72 mF.cm^{-2} , respectively. The hybrid material obeys the general characteristic of electrochemical capacitors, where the capacitance decreases with increasing current densities.

Figure 3.16 (a) and (b) shows the EIS data of the three materials, with the respective values of the ESR summarized in Table 3.3. The lowest ESR was recorded for the nCoTCPc/MWCNT. From the Bode plots, the phase angles were lower than the ideal -90° for an ideal EDLC, again proving the pseudocapacitive behavior of the thin films. The knee frequency (f_0 , $\phi=-45^\circ$) is the maximum frequency at which the capacitive behavior is dominant, and describes the power capability of a supercapacitor; the higher the f_0 the more rapidly the supercapacitor can be charged and discharged or the higher the power density that can be

achieved from the supercapacitor. The nCoTCPc gave the highest knee frequency with a time constant of 0.83 ms. This result shows that most of the stored energy is accessible up to this frequency.

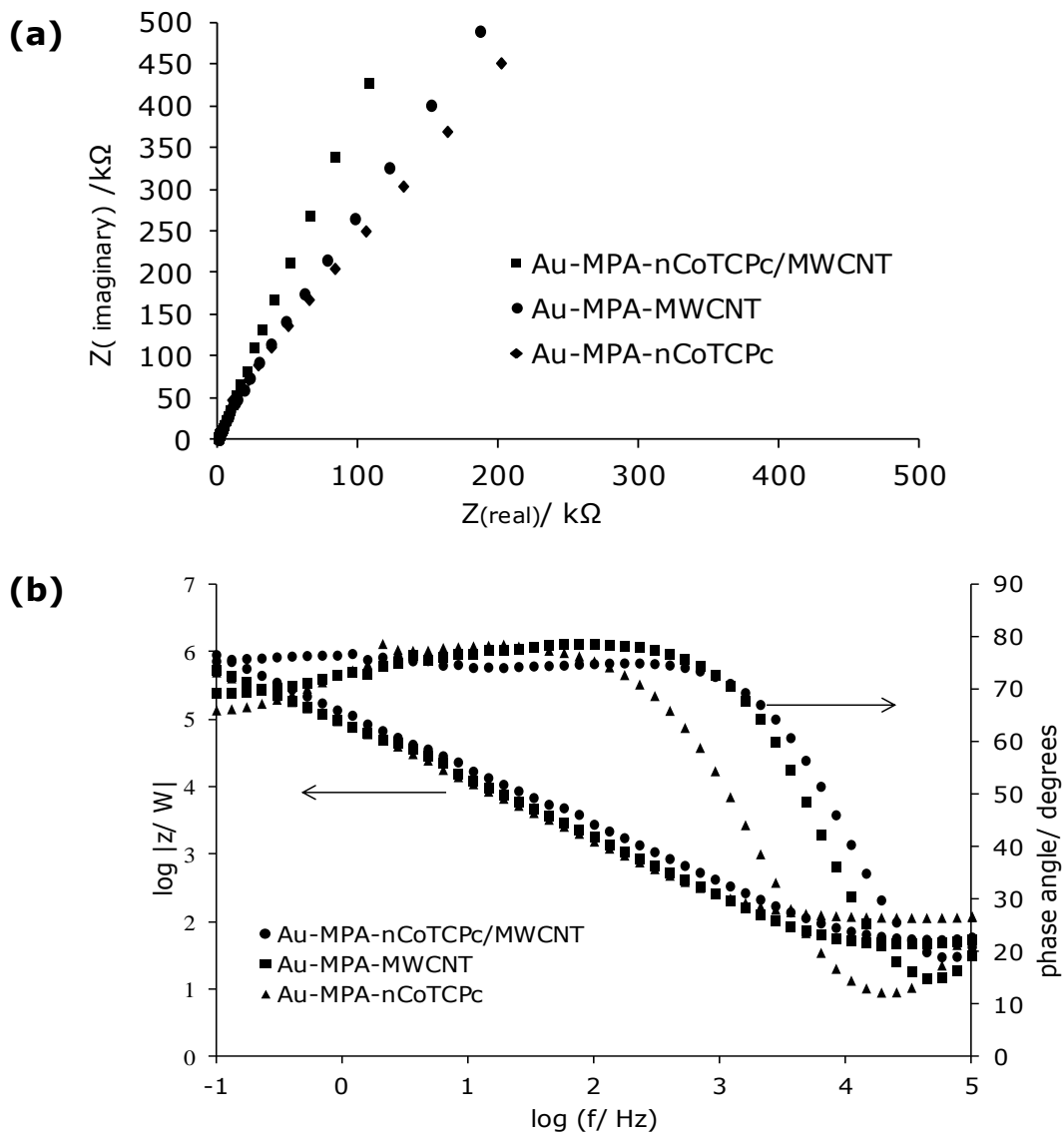


Figure 3. 16 Typical (a) Nyquist plot and (b) Bode plots for MWCNT, nCoTCPc and nCoTCPc/MWCNT

The energy deliverable efficiency (η / %) was obtained from Equation 3.7:

$$\eta(\%) = \frac{t_d}{t_c} \times 100 \quad (\text{Equation 3.7})$$

where t_d and t_c are discharge time and charging time, respectively. Figure 3.17 shows the energy deliverable efficiency and stability of the nCoTCPc/MWCNT upon continuous cycling (1000 cycles lasting 72 hrs) at a current density of $10 \mu\text{A}\cdot\text{cm}^{-2}$. There is minimal loss in capacitance over the first 200 cycles, thereafter the electrode shows loss in capacitance up to 600 cycles; further charge/discharge cycles do not result in loss of capacitance.

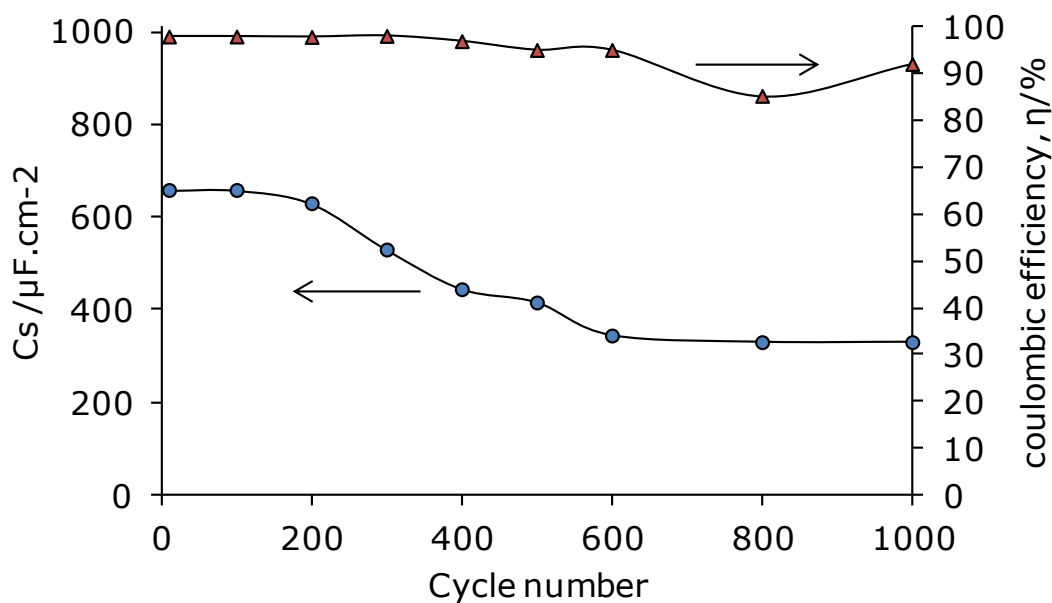


Figure 3. 17 Stability and efficiency plots of the gold electrode modified with nCoTCPc/MWCNT obtained at $10\mu\text{A}\cdot\text{cm}^{-2}$ in $1.0 \text{ M H}_2\text{SO}_4$

(b) ELECTROCATALYTIC DETECTION

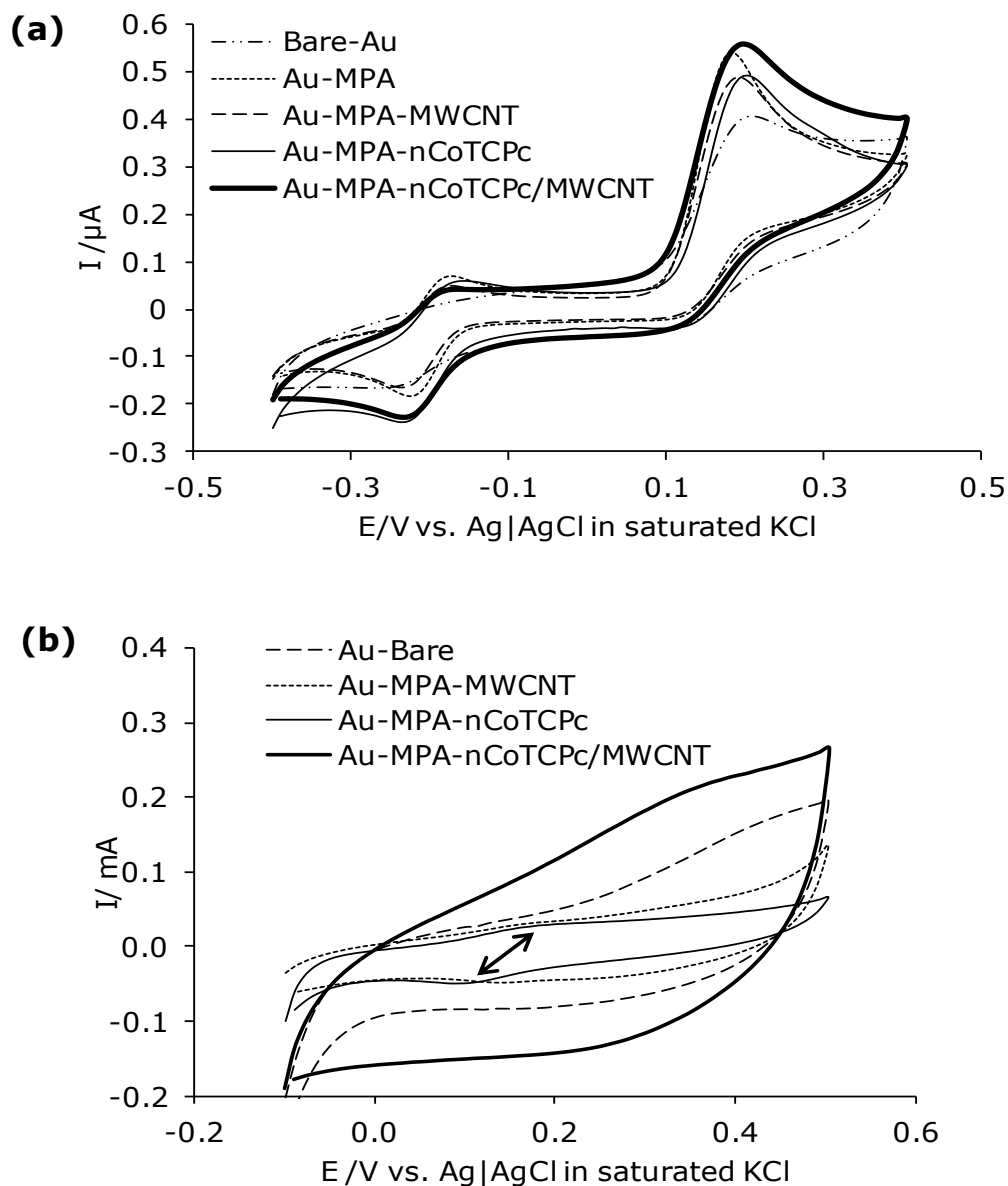


Figure 3. 18 Cyclic voltammetric profiles of the different electrodes in (a) presence and (b) absence of $50 \mu\text{M}$ EP in pH 7.4 PBS at a scan rate of $25 \text{ mV}\cdot\text{s}^{-1}$



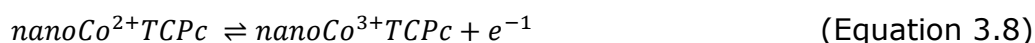
To determine the electrocatalytic properties, we investigated the electrochemical response of the nCoTCPc/MWCNT hybrid towards EP. The CV profiles, in Figure 3.18 (a), of the modified electrodes towards 50 μM EP in PBS show the following trend: Au-MPA-nCoTCPc/MWCNT ($I_p = 0.56 \mu\text{A}$) > Au-MPA ($I_p = 0.50 \mu\text{A}$) > Au-MPA-MWCNT ($I_p = 0.45 \mu\text{A}$) \approx Au-MPA-nCoTCPc ($I_p = 0.3 \mu\text{A}$). All CVs show the typical epinephrine redox process, with one irreversible peak at the anodic window and one reversible couple at the cathodic window ^[140-141]. Briefly, the anodic peak (+0.182 V) corresponds to the oxidation of epinephrine to the open-chain quinone while the peak observed at -0.228 V relates to the reduction adrenochrome to leucoadrenochrome. Continuous scanning resulted in a new oxidative reaction (-0.188 V) which corresponds to the oxidation of leucoadrenochrome to adrenochrome.

Interestingly, the Au-MPA shows enhanced current response in comparison to the equivalent peak current of Au-MPA-nCoTCPc and Au-MPA-MWCNT. This could be due the electrostatic attraction of the EP cations to the electrode surface, by the deprotonated MPA carboxyl groups. The slightly higher current response observed using Au-MPA-nCoTCPc/MWCNT in comparison to the other prepared electrodes is indicative of the superior electrocatalytic ability of the nanohybrid species. This synergistic effect may be credited to the electron-dense tube (integration of nCoTCPc and MWCNT) which facilitates the electron movement from the bulk to the electrode surface.

The CV responses (Figure 3.18 (b)) of Bare-Au, Au-MPA-nCoTCPc and Au-MPA-nCoTCPc/MWCNT were investigated in PBS pH 7.4, to determine the redox



contribution of the modified species. Bare-Au shows no current response while Au-MPA-nCoTCPc shows a redox process in the region of +0.16 V (indicated by the double arrow, attributed to the $\text{Co}^{2+}/\text{Co}^{3+}$, generally known for its weak appearance [142]). The $\text{Co}^{2+}/\text{Co}^{3+}$ redox process of the nCoTCPc species may be described as follows:



The Au-MPA-MWCNT also shows a weak response in the same region of +0.16 V. Compton's group attributed this occurrence to the presence of surface oxo-groups introduced during the functionalization process. Therefore, the ill-defined, quasi-reversible redox peak of the nCoTCPc/MWCNT complex observed at ~ 0.4 V may be as a result of the quinonyl oxygen functionalities of the acid functionalized MWCNTs [143-144] as well as the $\text{Co}^{2+}/\text{Co}^{3+}$ redox process of the nCoTCPc species.

To determine the electron transfer process at a constant concentration of 50 μM EP in PBS, we investigated the scan rate using Au-MPA-nCoTCPc/MWCNT. From the scan rate CV evolutions (Figure 3.19 (a)), the plot of peak anodic current (I_p) vs. square root of scan rate ($v^{1/2}$) (Figure 3.19 (b)), showed a linear relationship ($R^2 = 0.996$) with approximately zero intercept between 0.025 – 0.2 $\text{V}\cdot\text{s}^{-1}$ which is indicative of a diffusion-controlled process [145]. Higher scan rates ($> 0.2 \text{V}\cdot\text{s}^{-1}$), gave a straight line ($R^2 = 0.993$) with a negative intercept, suggesting that the reaction is not totally diffusion controlled but involves the adsorption of



intermediate products. With increasing scan rates, the oxidation peak potential shifts towards a more positive potential, confirming the kinetic limitation of the electrochemical reaction ^[146]. From the Tafel equation (Equation 3.9) for an irreversible diffusion controlled process, the linear relationship between anodic peak potential (E_{pa}) and $\log v$ (Figure 3.19 (c)) confirms chemical irreversibility of the EP electro-oxidation process. From the equation:

$$E_{pa} = \frac{b}{2} \log v \left(b = \text{Tafel slope} = \frac{0.059}{\alpha n_{\alpha}} \right) \quad (\text{Equation 3.9})$$

where n_{α} is the number of electrons involved in the process while α is the electron transfer coefficient. From the linear regression equation of $E_{pa} = 0.2389 + 0.0299 \log v$ ($R^2 = 0.988$), the Tafel slope = 0.0598 V/decade and $\alpha \approx 0.5$. A Tafel slope close of 0.059 V/decade is indicative of a 2 electron process; a fast catalytic redox process as the first step followed by a non-redox rate-determining step such as analyte binding with the catalyst or possible deprotonation of the analyte ^[147-148] as a possible mechanism. The catalyst redox process could be the $\text{nanoCo}^{2+}\text{TCPc}$ to $\text{nanoCo}^{3+}\text{TCPc}$ redox process followed by rate determining chemical step involving possible pi-pi interaction between $\text{nanoCo}^{3+}\text{TCPc}$ / MWCNT and EP molecule.

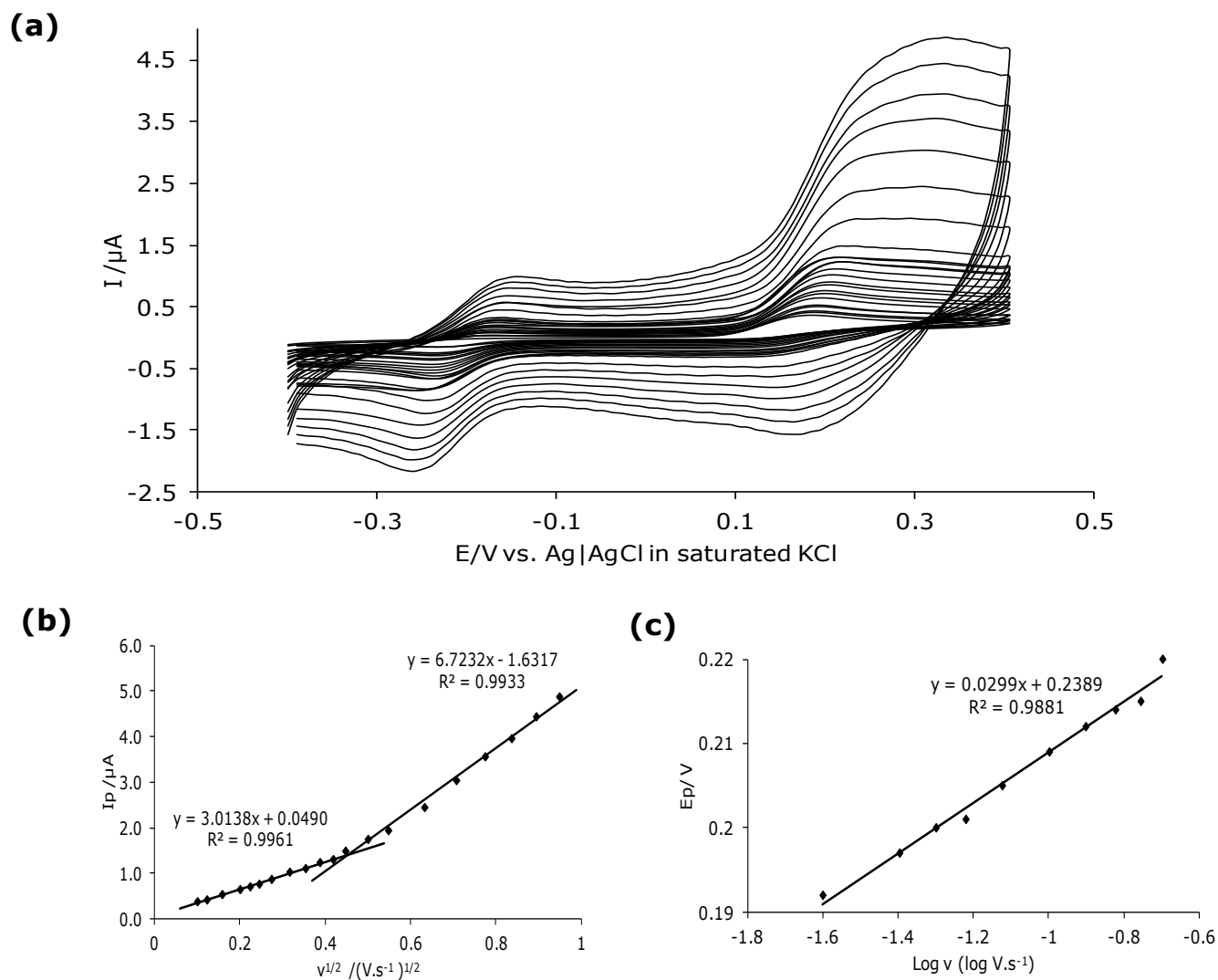


Figure 3. 19 (a) Cyclic voltammograms of increasing scan rates (5 – 300 mV.s^{-1}) for 10 mM EP in PBS pH 7.4 for Au-MPA-nCoTCPC/MWCNT (b) Plot of peak current (I_p) vs. square root of scan rate ($v^{1/2}$) and (c) plot of peak potential (E_p) vs. log of scan rate (v) from scan rate data



LIMIT OF DETECTION INVESTIGATION

As the nCoTCPc/MWCNT showed great current response and sensitivity, a further chronoamperometric study was employed to determine the limit of detection. This experiment was performed in EP in pH 7.4 PBS. Figure 3.20 shows the chronoamperogram that was obtained for a series of EP concentrations (0.47–4.12 μM). Golabi et. al. ^[149] reported kinetic limitation at high concentrations at a time interval of 30 s. We used a time interval of 1.2 s (fastest part of the reaction), where concentration is not governed by the kinetic aspect of the system. From the current responses of Au-MPA-nCoTCPc/MWCNT to the changes in the EP concentration, the limit of detection ($\text{LoD} = 3.3s/m$) ^[150], where s is the standard deviation of the intercept and the sensitivity, m (plot of linear peak current vs. the concentration of EP – Figure 3.20), were calculated to be ~ 280 nM and 7.03×10^{-3} A M^{-1} , respectively. This was compared to literature reports ^[151] on the electrocatalytic detection of EP (Table 3.5) and observed that our results exhibited comparable sensitivity with lower detection limits. This means SAM modified nCoTCPc/MWCNT on gold electrode is a promising platform for potential development of electrochemical sensing devices.

We also investigated the catalytic rate constant and diffusion coefficient of EP over a concentration range (1.30–3.55 μM). At intermediate times (0.0–2.0 s) of the chronoamperometric measurements, the catalytic currents (I_{cat}) were dominated by the rate of the electrocatalysed oxidation of EP, thus the rate constants for the chemical reactions between the biological analyte and redox sites of surface immobilised nCoTCPc/MWCNT Equation 3.3:



From the slopes of the plots of I_{cat}/I_L vs. $t^{1/2}$, over the concentration range 1.30 – 3.55 μM , the value of k was found to be $17.88 \times 10^6 \text{ cm}^3 \text{ mol}^{-1} \text{ s}^{-1}$ ($17.88 \times 10^3 \text{ M}^{-1} \text{ s}^{-1}$) for epinephrine. Our results are approximately equal to that ($16.24 \times 10^3 \text{ M}^{-1} \text{ s}^{-1}$) reported by Ardakani et. al [152] for the oxidation of EP at gold modified electrode but lower than a recent study ($22.00 \times 10^6 \text{ cm}^3 \text{ mol}^{-1} \text{ s}^{-1}$) using bulk CoTSPc/MWCNT on GCE [153]. This further confirms the nano-form of metallophthalocyanines offers improved electrocatalytic properties when compared to the bulk. The diffusion coefficient, D , was determined using the chronoamperometric data and the Cottrell equation represented in Equation 3.2.

The diffusion coefficient was calculated to be $2.51 \times 10^{-6} \text{ cm}^2 \text{ s}^{-1}$. Our results show a faster rate of diffusion when compared to other modified electrodes for the electro-oxidation of EP. The diffusion coefficient for benzohydrazide SAM modified gold electrode and modified carbon paste electrode were reported to be $3.60 \times 10^{-6} \text{ cm}^2 \text{ s}^{-1}$ [154] and $4.67 \times 10^{-6} \text{ cm}^2 \text{ s}^{-1}$ [155], respectively.

Table 3. 5 Comparative analytical data for the detection of epinephrine using electrochemical techniques

Electrode modification Materia	Electrolyte	Line range of EP (mol.L-1)	Detection Limit (mol.L-1)	Sensitivity	Ref
Au-DMAET-Cobalt tetraaminophthalocyanine	PBS, pH 7.0	12×10^{-6} - 133×10^{-6}	6×10^{-6}	9.4×10^{-3} AM^{-1}	[156]
Au-2-(2,3-dihydroxyphenyl)-1,2-dithiane	PBS, pH 7.0	0.7×10^{-6} - 500×10^{-6}	0.5×10^{-6}	0.01 M^{-1}	[157]
Au-2-hydroxy-N'1-[(E)-1-(3-methyl-2-thienyl)-methylidene] benzohydrazide	PBS, pH 6.0	3×10^{-6} - 100×10^{-6}	0.08×10^{-6}	$0.018 \mu\text{A}$ μM^{-1}	[158]
Au-4-nitrothiophenol/4-mercaptobenzoic acid	PBS, pH 6.5	0.1×10^{-6} - 2×10^{-6}	0.04×10^{-6}	1.2 AM^{-1}	[159]
Au-Polypyrrole/gold nanoparticle/SWCNT hybrid film	PBS, pH 7.0	4×10^{-9} - 1.0×10^{-7}	2.0×10^{-9}	-	[160]
Au-Gold nanoparticle-dithiodipropionic Acid-cysteamine-gold nanoparticles	PBS, pH 7.0	1.0×10^{-7} - 7.5×10^{-7}	8.2×10^{-8}	-	[161]
Au-Cysteine-Metallophthalocyanine) complexes	PBS, pH 7.4	Up to 300 $\times 10^{-9}$	13.8×10^{-9}	0.53 nA nM^{-1}	[162]
Au-dithiothreitol/dodecanethiol/ gold nanoparticle composite	PBS, pH 7.0	10^{-7} - 10^{-6}	60×10^{-9}	0.33 mA mM^{-1}	[163]
Au-Penicillamine	PBS, pH 7.0	5×10^{-7} - 10^{-6}	0.1×10^{-6}	0.052 mA mM^{-1}	[164]
Au-3Mercaptopropionic acid	PBS, pH 6.8	2×10^{-7} - 10^{-6}	100×10^{-9}	-	[165]
Au-L-cysteine-aminylferrocene	PBS, pH 7.4	1.7×10^{-7} - 10^{-4}	18×10^{-9}	0.92 mA mM^{-1}	[166]

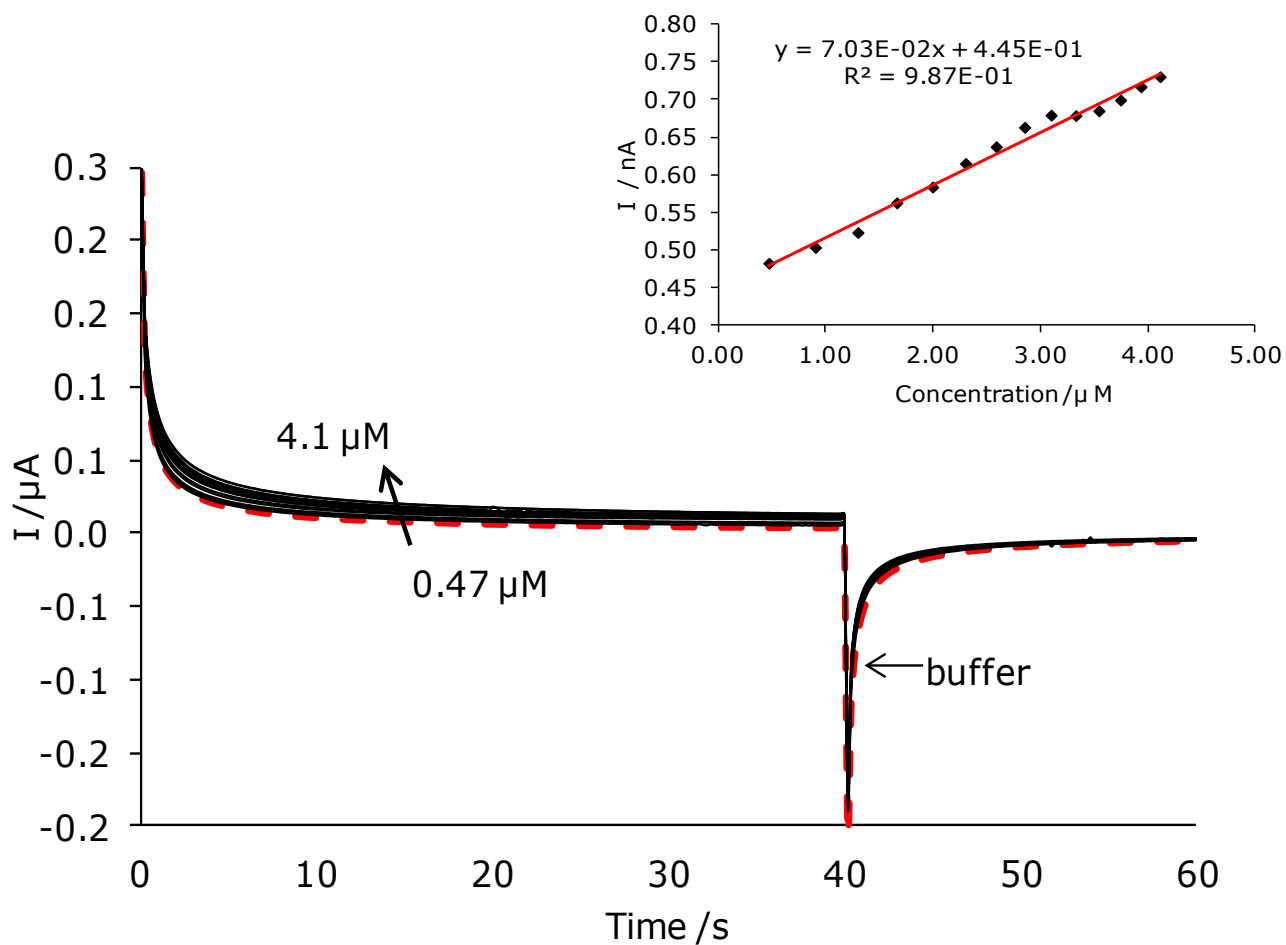


Figure 3. 20 Typical double potential step chronoamperometric at Au-MPA-nCoTCPc/MWCNT in pH 7.4 PBS solution following addition of epinephrine. Concentration range (0.47–4.12 μM). Insert shows the plot of chronoamperometric current at $t = 1.2$ s vs. $[\text{EP}]$ at scan rate $25 \text{ mV}\cdot\text{s}^{-1}$



CONCLUSIONS AND RECOMMENDATIONS



CONCLUSION

This thesis describes the synthesis of three nanohybrids. The main methods of synthesis included:

- (i) In situ addition in which AuNP were synthesised onto MWCNT (AuNP/MWCNT)
- (ii) Sonication of bulk components to induce electrostatic attachment (AuNR/MWCNT)
- (iii) Sonication of bulk components dissolved in acid into their nanoform whilst inducing an electrostatic attachment to MWCNT (nCoTCPC/MWCNT)

The hybrids formed displayed new physical and electrochemical characteristics in comparison to their individual bulk components. The AuNP/MWCNT hybrid did not perform as expected and therefore was not fully investigated. However the remaining 2 hybrids were analysed and compared. The AuNR/MWCNT was larger in size due to the CTAB, which held the hybrid together. The nCoTCPC/MWCNT hybrid formed a “rope like structure” that was bulkier and more soluble in solution than the individual components.

Further electrocatalytic analysis showed that the AuNR/MWCNT hybrid had lower electrocatalytic abilities than the nCoTCPC/MWCNT hybrid. The I_p for EP in pH 7 PBS was 0.48 μA and 0.56 μA for the AuNR/MWCNT and nCoTCPC/MWCNT hybrids respectively. The same trend was seen for the chronoamperometric studies, the LoD 's was 0.5 s/m and 3.3 s/m for the AuNR/MWCNT and nCoTCPC/MWCNT respectively. Overall the electrocatalytic ability of the



nCoTCPc/MWCNT hybrid species was significantly higher than that of the AuNR/MWCNT hybrid.

The nCoTCPc/MWCNT was a novel hybrid that has not been previously reported in literature. Extensive characterisation showed that the nCoTCPc/MWCNT nanohybrid material exhibited faster electron transfer and higher charge storage properties than its individual species. The nCoTCPc/MWCNT hybrid showed excellent charge storage efficiency as it maintained columbic efficiency for approximately 1000 cycles. The nanoCoTCPc/MWCNT nanohybrid material promises to serve as a potential material for the fabrication of thin film electrocatalysts and pseudocapacitors.

From the results obtain it can be deduced that the optimised pairing of material into nanohybrids can form species with advanced electrocatalytic and charge storage abilities when compared to their individual bulk components.



RECOMMENDATIONS

- Enhanced studies of AuNP and AuNR and their modes and methods of attachment to MWCNT should be conducted.
- Other bulk electrodes should be investigated for optimised electrocatalytic detection.
- Assembly of multiple layers onto the electrode should be investigated as it could show greater analyte detection thus higher sensitivity with a lower limit of detection



REFERENCES

1. R. G. Compton, C. E. Banks, Understanding Voltammetry, World Scientific Publishing Co., Singapore, 2007.
2. A. E. Kaifer, M. Gomez-Kaifer, Supramolecular Electrochemistry, Wiley-VCH, New York, 1999.
3. J. Wang, Analytical Electrochemistry, VCH Publishers Inc., New York, 1994.
4. A. J. Saleh Ahammad, J. Lee, Md. A. Rahman, Sensors 9 (2009) 2289.
5. R. P. Olenick, T. M. Apostol, D. L. Goodstein, beyond the mechanical universe: from electricity to modern physics, Cambridge university Press, 1986, ISBN 0-521-30430-X p.160
6. S. Weinberg, The discovery of subatomic particles, Cambridge University Press, 2003, ISBN 0-521-82351-X p.15
7. A. K. Shukla, T. P. Kumar, Central Electrochemical research institute, Pillars of Modern Electrochemistry: A brief History, India, 2008.
8. K. J. Laidler, The world of Physical chemistry, Oxford University Press ,1995, 219.
9. H. Luo, Z. Shi, N. Li, Z. Gu, Q. Zhaung, Anal. Chem. 73 (2001) 915.
10. F. Lucarelli, G. Marrazza, A. P. F. Turner, M. Mascini, Biosensors and bioelectronics 19 (2004) 515.
11. C. N. Svendsen, Analyst 118 (1993) 123.
12. K. B. Prater, A. J. Bard, J. Electrochem. Soc. 117 (1970) 207.
13. V. J. Puglisi, A. J. Bard, J. Electrochem. Soc. 119 (1972) 883.



14. J.O'M Bockris, S. U. Khan, Surface Electrochemistry: A Molecular Level Approach. New York: Plenum Press, 1993.
15. D. A. Skoog, F. J. Holler, T. A. Nieman, Principals Of Instrumental Analysis, 5th ed., Harcourt Brace College Publishers, 1998, 639.
16. D. B. Hibbert, Introduction to Electrochemistry, Macmillan, London, 1993.
17. I. M. Kolthoff, W. J. J. Tomsicek, Phys. Chem. 39 (1935) 945.
18. M. V. Reddy, B. Pecquenard, P. Vinatier, A. Levasseur, Electrochemistry Communications 9 (2007) 409.
19. A. J. Bard, L. R. Faulkner, Electrochem methods: Fundamentals and applications, 2nd ed., John Wiley & sons, Hoboken, NJ, 2001.
20. J. Wang, Analytical Electrochemistry, VCH Publishers INC., New York, 1994.
21. J. E. B. Randles, Trans. Faraday Soc. 1978, 44, 327.
22. K. J. Laidler, The world of Physical chemistry, Oxford University Press, 1995, 219.
23. D. M. Anjos, J. K. McDonough, E. Perre, G. M. Brown, S. H. Overburg, Y. Gogotsi, V. Presser, nano energy (2013).
24. K. I. Ozoemena, T. Nyokong, Microchemical Journal 75 (2003) 241.
25. B. Agboola, T. Nyokong, Talanta 72 (2007) 691.
26. K. A. Joshi, M. Prouza, M. Kum, J. Wang, J. Tang, R. Haddon, W. Chen, A. Mulchandani, Anal. Chem. 78 (2006) 331.
27. Raistrick, I. D.; Franceschetti, D. R.; and Macdonald, J. R. Chapter 2: Theory, page 37, in Impedance Spectroscopy: Theory, Experiment and



-
- Applications, edited by E. Barsoukov and J. R. Maconald. John Wiley & Sons, Inc., Hoboken, New Jersey, 2005.
28. S. Kraus in: A. J. Bard, M. Stratmann, P. R. Ulwin (Eds.), Instrumental and Electroanalytical chemistry , Wiley-GmbH & Co., 2003.
 29. W. A. Badawy, K. M. Ismail, M. Medany, Int. J. Electrochem. Sci., 2011, 6.
 30. H. Goto, S. Nimori, Journal of Material Chemistry 20 (2010) 1891.
 31. G. Hager, A. G. Brolo, Journal of Electroanalytical Chemistry 550 (2003) 291.
 32. R. Yamada ,K. Uosaki, Langmuir 13 (1997) 5218.
 33. R. Yamada , K. Uosaki, Langmuir 14 (1998) 855.
 34. B. Šustrová, K. Štulík,V. Mareček, Int. J. Electrochem. Sci. 8 (2013) 4367.
 35. S. Varatharajan, S. Berchmans, V. J. Yegnaraman, Chem. Sci. 121 (2009) 665.
 36. Z. Li, T. Niu, Z. Zhang, S. Bi, S. Electrochimical acta 55 (2010) 6907.
 37. J. Pillay, K. I. Ozoemena, R. T. Tshikhudo, R. M. Moutloali, Langmuir 26 (2010) 9061.
 38. K. I. Ozoemena, D. Nkosi, J. Pillay, Electrochimica Acta 53 (2008) 2844.
 39. K. I. Ozoemena, T. Nyokong, Microchemical Journal 75 (2003) 241.
 40. T. H. Tsai, S. Thiagarajan, S. M. Chen, C. Y. Cheng, Thin Solid Films 530 (2013) 3054.
 41. H. Luo, Z. Shi, N. Li, Z. Gu, Q. Zhaung, Anal. Chem. 73 (2001) 915.
 42. J. K. Yao, H. Shao, Journal of the Chinese Chemical Society 52 (2005) 363.



-
43. V. Ganesh, S. K. Pal, S. Kumar, V. Lakshminarayanan, *Journal of Colloid and Interface Science* 296 (2006) 195.
 44. J. Kreuter, *International Journal of pharmaceuticals* 331 (2007) 1.
 45. N. Taniguchi, "On the Basic Concept of 'Nano-Technology'," *Proc. Intl. Conf. Prod. Eng. Tokyo, Part II, Japan Society of Precision Engineering, 1974*
 46. M. Robertson, *Chemistry world* (2010) 48.
 47. A. S. Thakor, J. Okerst, C. Zavaleta, T. F. Massoud, S. S. Bambhir, *Nanoletters* (2011).
 48. MLA style: "Richard Zsigmondy - Biographical". Nobelprize.org. Nobel Media AB 2013. Web. 6 May 2014. <http://www.nobelprize.org/nobel_prizes/chemistry/laureates/1925/zsigmondy-bio.html>
 49. M. Brust, M. Walker, D. Bethell, D. J. Schiffrin, R. Whyman, *J. Chem. Soc. Chem. Commun.* 7 (1994) 801.
 50. B. V. Enustun, J. Turkevich, *J. Am. Chem. Soc.* 85 (1963) 3317.
 51. J. Kimling, M. Maier, B. Okenve, V. Kotaidis, H. Ballot, A. Plech, *American Journal of Phys. Chem. B* 110 (2006) 15700.
 52. B. Nikoobakht, M. A. El-Sayed, *Chem. Mater.* 15 (2003) 1957.
 53. H. Huang, C. He, Y. Zeng, X. Xia, X. Yua, P. Yi, Z. Chen, *Journal of Colloid and Interface Science* 322 (2008) 136.
 54. J. Pérez-Juste, I. Pastoriza-Santos, L. M. Liz-Marzána, P. Mulvaney, *Coordination Chemistry Reviews* 249 (2005) 1870.



-
55. P.R. Selvakannan, E. Dumas, F. Dumur, C. Péchoux, P. Beaunier, A. Etcheberry, F. Sécheresse, H. Remita, C. R. Mayer, *Journal Of Colloid And Interface Science* 349 (2010) 93.
 56. S. P Fricker, *Gold Bull.* 29 (1996) 53.
 57. C. You, A. Chompoosor, V.M. Rotello, *Nanotoday* 2 (2007) 34.
 58. A. Verma, V.M. Rotello, *Chem. Commun.* 3 (2005) 303.
 59. T. Niidome, A. Ohga, Y. Akiyama, K. Watanabe, Y. Niidome, T. Mori, Y. Katayama, *Bioorganic & Medicinal Chemistry* 18 (2010) 4453
 60. M. Nithyapriya, C. Chellaram, *Indian Journal of Innovations and developments*, 1 (2012)
 61. K. Ozoemena, T. Nyokong, *J. Chem. Soc. Dalton Trans.*3 (2002) 1806–1811.
 62. H. P. Boehm, *Carbon* 35 (1997) 581.
 63. M. Monthioux, V. Kuznetsov, *Carbon* 44 (2006) 1621.
 64. S. Iijima, *Nature* 354 (1991) 56.
 65. M. Monthioux, J. Spreadborough, *Nature* 186 (1960) 29.
 66. P.G. Wiles, J. Abrahamson, *Carbon* 16 (1978) 341.
 67. A. Oberlin, M. Endo, T. Koyama, *Journal of Crystal Growth* 32 (1976) 335.
 68. Hughes T.V, Chambers C.R. US Patent 405480, 1889.
 69. H. Kroto, J. Heath, S. O'Brien, R. Curl, R. Smalley, *Nature* 318 (1985) 162.
 70. S. Iijima, *Journal of Crystal Growth* 50 (1980) 675.
 71. *Izvestiya Akademii Nauk SSSR* 3 (1982) 12.
 72. S. Iijima, T. Ichihashi, *Nature* 363 (1993) 603.



-
73. J. W. Mintmire, B. I. Dunlap, C. T. White, *Physical Review Letter* 68 (1992) 631.
 74. D. S. Bethune, C. H. Kiang, M. S. De Vries, G. Gorman, R. Savoy, J. Vazquez, R. Beyers, *Nature* 363 (1993) 605.
 75. A. Thess, R. Lee, P. Nikolaev, H. Dai, P. Petit, J. Robert, C. Xu, Y. H. Lee, S. G. Kim, A. G. Rinzler, D. T. Colbert, G. E. Scuseria, D. Tomane´k, J.E. Fischer, R.E. Smalley, *Science* 273 (1996) 483.
 76. J. W. Mintmire, *Physical Review Letters* 68 (1992) 631.
 77. R. Pfeiffer, T. Pichler, Y. A. Kim, H. Kuzmany, *Topics in Applied Physics* 111(2008) 495.
 78. J. Despres, E. Daguerre, K. Lafdi, *Carbon* 33 (1995) 87.
 79. C. P. Poole Jr., F. J. Owens, *Introduction to Nanotechnology*, John Wiley and Sons Inc., Hoboken, New Jersey, 2003.
 80. S. Kawasaki, Y. Iwai, M. Hirose, *Carbon* 47 (2009) 1081.
 81. S. Iijima, *Nature* 354 (1991) 56.
 82. Y. K. Kwon, D. Tomanek, *The American Physical Society* 58 (1998) 57.
 83. S. R. Malik, M. A. Maqbool, S. Hussain, H. Irfan, *J Pak Material Society* 2 (2008) 21
 84. R.A Jishi, M.S. Dresselhaus, G. Dresselhaus, *Matter and Materials Physics* 47 (1993) 16671.
 85. M.S. Strano, C.A. Dyke, M.L. Usrey, P.W. Barone, M.J. Allen, H. Shan, C. Kittrell, R.H. Hauge, J.M. Tour, R.E. Smalley, *Science* 301 (2003) 1519.



-
86. P. J. F. Harris, Carbon nanotubes and related structures; new material for the 21s century (1957) 5.
 87. J. Tersoff, R. S. Ruoff, Physical Review Letters 73 (1994) 676.
 88. H. Dai, Surface Science 1 (2002) 218.
 89. J. Lui, A. G. Rinzler, H. Dai, J. H. Hafner, R. K. Bradley, P. J. Boul, A. Lu, T. Iverson, K. Shelimov, C. B. Huffman, F. Rodriguez-Macias, Y. Shon, T. R. Lee, D. T. Colbert, R. E. Smalley, Science 280 (1998) 1253.
 90. P. J. Britto, K. S. V. Santhanam, P. M. Ajayan, Bioelectronics and Bioenergetics 41 (1996) 121.
 91. H. Luo, Z. Shi, N. Li, Z. Gu, Q. Zhuang, Anal. Chem. 73 (2001) 915.
 92. Ahmed Galal*, Nada F. Atta, Ekram H. El-Ads Talanta 93 (2012) 264.
 99. J. Huang, X. Xing, X .Zhang, X. He, Q. Lin, W. Lian, H. Zhu, Food Research International 44 (2011) 276.
 94. A. Braun, J. Tcherniac, Berichte der Deutschen Chemischen Gesellschaft 40 (1907) 2709.
 95. H. de Diesbach, E. von der Weid, Helevtica Chimica Act 10 (1927) 886.
 96. P.Gregory, J. Porphyrins, Phthalocyanines 3 (1999) 468.
 97. Sappok, R. J.O.C.C.A., 61 (1978) 299.
 98. R.P. Linstead, J. Chem. Soc. (1934) 1016.
 99. J.M. Roberston, J. Chem. Soc. (1935) 615.
 100. J.M. Roberston, J. Chem. Soc. (1936) 1195.
 101. M.P. Somashekarappa, K.R. Venugopala Reddy, M.N.K. Harish, J. Keshavayya, Journal of Molecular Structure 753 (2005) 190.



-
102. Phthalocyanines: Properties and Applications, C.C. Leznoff and A.B.P.Lever, Eds., VCH Publishers, New York, 1-4, 1989, 1993, 1993, 1996.
 103. K.R. Venugopala Reddy, J. Keshavayya, Dyes and Pigments 53 (2002) 187.
 104. K.R. Venugopala Reddy, J. Keshavayya, Turk. J. Chem. 26 (2002) 573.
 105. M.P. Somashekarappa, J. Keshavayya, Synth. React. Inorg. Met.-Org.Chem. 31 (2002) 811.
 106. T. Enokida, R. Hirohashi, S. Mizukami, Journal Of Imaging Science 35 (1991) 235.
 107. T. Saito, T. Kawanishsi, A. Kakuta, Jpn. J. Appl. Phys. A 30 (1991) L1182.
 108. H. Z. Chen, K. J. jiang, M. Wangm S. L. yang, Journal Of Photochem. Photobiol. A 117 (1998) 149.
 109. Y. wang, K. deng, L. Gui, Y. Tang, J. Zhou, L. Cai, J. Qui, D. Ren, Y. Wang, Journal Of Colloidal Interface Science 213 (1999) 270.
 110. C. Hamann, A. Mrwa, Int. J. Electron. 73 (1992) 1039.
 111. T. Frauenheim, C. Hamann, M. Müller, Phys. Status Solidi A 86 (1984) 735.
 112. A. Ahmad, R.A. Collins, Thin Solid Films 217 (1992) 75.
 113. J. C. Hsieh, C. J. Liu, Y .H. Ju , Thin Solid Films 322 (1998) 98.
 114. F.H. Moser, A.L. Thomas, Phthalocyanines Compounds, Rehinhold Publishing Corporation, New York, 1963.



-
115. J. Ikhal, L.R. Fulkner, K. Dwarakanath, K. Tachikawa, J. Am. Chem. Soc. 108 (1986) 5434.
 116. C.C. Leznoff, A.B.P. Lever, Phthalocyanines, Properties And Applications, 1, VCH Publications, Inc., New York, 1989.
 117. P. Gregory, J. Porphyrins, Phthalocyanines 4 (2000) 432.
 118. K. Kudo, T. Sumitomo, K. Hiraga, S. Kuniyoshi, K. Tanaka, Jpn. J. Appl. Phys. Part 1 36 (1997) 6994.
 119. K.I. Ozoemena, T. Nyokong, in: C. A Grimes, E.C. Dickey, M.V. Pishko, (Eds.), Encyclopedia of Sensors Vol.3, Chapter E, pp.157 – 200, American Scientific Publishers, California, 2006.
 120. B. Sljukic, C. E. Banks, C Salter, A. Crossley, R. G. Crompton Analyst 131 (2006) 670.
 121. M. Siswana, K.I. Ozoemena, T. Nyokong, Talanta 69 (2006) 1136.
 122. J. Lui, A. G. Rinzler, H. Dai, J. H. Hafner, R. K. Bradley, P. J. Boul, A. Lu, T. Iverson, K. Shelimov, C. B. Huffman, F. Rodriguez-Macias, Y. Shon, T. R. Lee, D. T. Colbert, R. E. Smalley, Science 280 (1998) 1253.
 123. Z. Sun, X. Zhang, Y. Liang, H. Li, Journal of Power Sources 191 (2009) 366
 124. R. Zhang, M. Hummelgård, H. Olin, Materials science and engineering 158 (2009) 48.
 125. R. Zhang, M. Hummelgård, H. Olin, Materials science and engineering 158 (2009) 48.
 126. T. Niidome, A. Ohga, Y. Akiyama, K. Watanabe, Y. Niidome, T. Mori, Y. Katayama, Bioorganic & Medicinal Chemistry 18 (2010) 4453



-
- 127 Z. Sun, W. Ni, Z. Yang, X. Kou, L. Li, J. Wang, *small 4* (2008) 1287.
- 128 K. G. Thomas, S. Barazzouk, B. I. Ipe, S. T. S. Joseph, P. V. Kamat, *J. Phys. Chem. B* 108 (2004) 13066.
- 129 H.S. White, J. Leddy, A.J. Bard, *J. Am. Chem. Soc.* 104 (1982) 4811.
- 130 E. Laviron, *J. Electroanal. Chem.* 101 (1979) 19.
- 131 B. Zeng, Y. Yang, F. Zhao, *Electroanalysis* 15 (2003) 1054
- 132 L. Wang, J. Bai, P. Huang, H. Wang, L. Zhang, Y. Zhao, *Electrochem. Commun.* 8 (2006)1035.
- 133 M. J. Giz, B. Duong, N. J. Tao, *J. Electroanal. Chem.* 465 (1990) 72.
- 134 L. Yang, Y. Li, *Biosens. Bioelectron.* 20 (2010) 1407.
- 135 I.D. Raistrick, D.R. Franceschetti, J.R. Macdonald, in: E. Barsoukov, J.R. Macdonald (Eds.), *Impedance Spectroscopy: Theory Experiment and Applications*, 2nd Ed., Wiley, Hoboken, NJ, 2005.
- 136 C. A. Thorogood, G. G. Wildgoose, A. Crossley, R.M.J. Jacobs, J.H. Jones, R.G. Compton, *Chem. Mater.* 19 (2007) 4964.
- 137 C.A. Thorogood, G. G. Wildgoose, J.H. Jones, R.G. Compton, *New J. Chem.* 31 (2007) 958.
- 138 R. Signorelli, D. C. Ku DC, J. G. Kassakian, J. E. Schindall, *Institute of Electrical and Electronics Engineers* 97 (2009) 1837.
- 139 Y. Jiang, A. Kozinda, T. Chang, L. Lin, *Sensors and Actuators A* 195 (2013) 224.
140. M.D. Hawley, S.V. Tatawawadi, S. Piekarski, R.N Adams *J. Am. Chem. Soc.* 89 (1967) 447.



-
141. H.S. Wang, D.Q. Huang, R.M. Liu, J. Electroanal. Chem. 570 (2004) 528.
 142. S. Griveau, J. Pavez, J.H. Zagal, F. Bedoui, J. Electroanal. Chem. 497 (2001) 75.
 143. C. A. Thorogood, G. G. Wildgoose, A. Crossley, R.M.J. Jacobs, J.H. Jones, R.G. Compton, Chem. Mater., 19 (2007) 4964.
 144. C.A. Thorogood, G. G. Wildgoose, J.H. Jones, R.G. Compton, New J. Chem., 31 (2007) 958.
 145. H.S. White, J. Leddy, A.J. Bard, J. Am. Chem. Soc. 104 (1982) 4811.
 146. E. Laviron, J. Electroanal. Chem. 101 (1979) 19.
 147. J.H. Zagal, S. Lira, S. Ureta-Zanartu, J Electroanal Chem 210 (1986) 95.
 148. J.P. Collman, M. Kaplun, C.J. Sunderland, R. Boulatov, J. Am. Chem. Soc. 126 (2004) 11166.
 149. S.M. Golabi, H.R. Zare, Journal of Electroanalytical Chemistry 465 (1999) 168.
 150. G.D. Christian, Analytical Chemistry, 6th ed., John Wiley and Sons, New York, 2004, p. 113.
 151. K.I. Ozoemena, D. Nkosi, J. Pillay, Electrochim. Acta 53 (2008) 2844.
 152. M. Ardakani, H. Beitollahi, M.K. Amini, B-F. Mirjalili, F. Mirkhalaf, Journal of Electroanalytical Chemistry 651 (2011) 243.
 153. X. Lu, Y.Li, J. Du, X. Zhou, Z. Xue, X.Liu, Z. Wang, Electrochimica Acta 56 (2011) 7261.
 154. Pillay, J.; Vilakazi, S. Journal of Porphyrins and Phthalocyanines 16 (2012) 785.



-
155. Z. Moghadam, S.M. Ghoreishi, M. Behpour, M. Motaghedifard, *Journal of the Electrochemical Society* 160 (2013) H126.
 156. K.I. Ozoemena, D. Nkosi, J. Pillay, *Electrochim. Acta* 53 (2008) 2844.
 157. M. Ardakani, H. Beitollahi, M.K. Amini, B-F. Mirjalili, F. Mirkhalaf, *Journal of Electroanalytical Chemistry* 651 (2011) 243.
 158. Z. Moghadam, S.M. Ghoreishi, M. Behpour, M. Motaghedifard, *Journal of the Electrochemical Society* 160 (2013) H126.
 159. A. Salimi, R. Hallaj, S. Soltanian, H. Mamkhezri, *Anal. Chim. Acta* 594 (2007) 24.
 160. B.O. Agboola, S.L. Vilakazi, K.I. Ozoemena, *Journal of Solid State Electrochemistry* 13 (2009) 1367.
 161. M. Ardakani, N. Rajabzadeh, A. Dehghani-Firouzabadi, M. Sheikh-Mohseni, A. Benvidi, H. Naeimi, M. Marzieh; A. Karshenas, *Analytical Methods* 4 (2012) 2127.
 162. B.O. Agboola, K.I. Ozoemena, *Electroanalysis* 20 (2008) 1696.
 163. L. Wang, J. Bai, P. Huang, H. Wang, L. Zhang, Y. Zhao, *Electrochem. Commun.* 8 (2006) 1035.
 164. L. Wang, J. Bai, P. Huang, H.Wang, L. Zhang, Y. Zhao, *Int. J. Electrochem. Sci.* 1 (2006) 238.
 165. B. Zeng, Y. Yang, F. Zhao, *Electroanalysis* 15 (2003) 1054.
 166. B. Fang, X.-H. Deng, X.-W. Kan, H.-S. Tao, W.-Z. Zhang, M.-G. Li, *Anal. Lett.* 39 (2006) 697.